

HYDROTHERMAL SYNTHESIS OF PYRITE PHASE THIN FILMS

AS
36
2019
CHEM
.M37

A thesis submitted to the faculty of
San Francisco State University
In partial fulfillment of
the requirements for
the Degree

Masters of Science

In

Chemistry

by

Diana Greenough Mars

San Francisco, California

January 2019

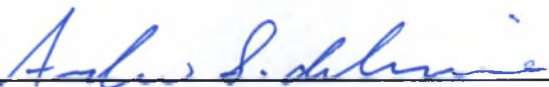
Copyright by
Diana Greenough Mars
2019

HYDROTHERMAL SYNTHESIS OF PYRITE PHASE THIN FILMS

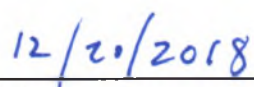
Diana Greenough Mars
San Francisco, California
2016

The pyrite phase of iron disulfide (FeS_2) has attracted interest as a visible light absorption layer for photovoltaic cells because of its low band gap and large absorption coefficient. A one-step hydrothermal approach was employed to synthesize pyrite thin films for solar applications. X-ray diffraction and scanning electron microscopy were used to characterize the films and confirm the presence of the pyrite phase. Films consisting of primarily the pyrite phase were synthesized, although crystal growth and surface roughness were difficult to control.

I certify that the Abstract is a correct representation of the content of this thesis.



Chair, Thesis Committee



Date

CERTIFICATION OF APPROVAL

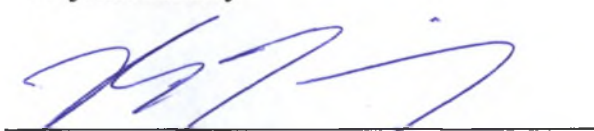
I certify that I have read Hydrothermal Synthesis of Pyrite Phase Thin Films by Diana Greenough Mars and that in my opinion this work meets the criteria for approving a thesis submitted in partial fulfillment of the requirement for the degree Master of Science in Chemistry at San Francisco State University.



Andrew S. Ichimura, Ph.D.
Associate Professor



Clive Hayzelden, D. Phil
Adjunct Faculty



Bruce A. Manning, Ph.D.
Associate Professor

ACKNOWLEDGEMENTS

I would first like to acknowledge my thesis advisor Dr. Andrew S. Ichimura of San Francisco State University. Dr. Ichimura's inexhaustible amount of patience and lack of judgement about the length of time I needed to complete this phase of my education has been invaluable in preventing me from giving up.

I would also like to acknowledge Dr. Clive Hayzelden of San Francisco State University for his exacting standards tempered by a dry wit that made the difficult task of writing a thesis funny and thus much less frightening. Also Dr. Bruce Manning for helping me repair all the technical difficulties I encountered while navigating the SFSU graduate program with good humor and a smile.

I would like to acknowledge Dr. Annette Chan for her unwavering encouragement and endless anecdotes of other people's experiences in graduate school that made me realize I am not alone in my apprehension.

There are a host of other folks who either influenced or helped me navigate a scientific education as an older student with an art background as well. From San Francisco State University: Dr. Frank T. Bayliss, Dr. Steven L. Weinstein, Dr. Diana S. Chu, and Dr. Carmen R. Domingo. From City College of San Francisco: Dr. Ronald Drucker, Dr. Timothy M. Su, and Drs. Lawrence K. Fong and Raymond H. Fong. From the San Francisco Art Institute: Timothy Berry, Tony Labat, Gordon Kluge and Kathy Acker. From the Cleveland Playhouse, Morgan Lund. Thank you all for your lasting mentorship.

Finally, I acknowledge a debt of gratitude to my friends and family who all believed I could do it: Nicole Diaconoff, Annelise DeVore, Larry and Susan Rakow, Henry and Rollie Hudson, Lizzy Caston, Carey Musgrave, and the Extended Ichimura Laboratory.

Diana G. Mars

TABLE OF CONTENTS

1	INTRODUCTION	1
1.1	Fossil Fuels for Energy Generation and Atmospheric CO ₂	1
1.2	Atmospheric CO ₂ and Climate Change	3
1.3	Light Induced Charge Separation in Semiconductors.....	4
1.4	Solar Cells	6
1.4.1	Polycrystalline Silicon (p-Si).....	8
1.4.2	Amorphous Silicon (a-Si).....	8
1.5	Semiconducting Thin Films	11
1.5.1	Cadmium Telluride Cells.....	12
1.5.2	Gallium Arsenide Cells.....	12
1.5.3	Dye Sensitized Cells	12
1.6	The Case for FeS ₂ Absorbers	14
1.6.1	Synthesis of Iron Sulfides	16
1.6.2	Metal-Organic Chemical Vapor Deposition.....	16
1.6.1	Sulfurization of Iron	17
1.6.2	Hot Injection	18
1.7	Low Temperature Synthesis and Research Goals	19
1.7.1	The Advantage of Hydrothermal Synthetic Methods.....	19
1.7.2	Research Goals	20
2	EXPERIMENTAL METHODS	20
2.1	Materials Synthesis	21
2.1.1	Precursor Method (M1)	21
2.1.2	Sulfate Salt Method (M2)	23
2.1.3	Preparation of Substrate.....	24
2.2	Materials Characterization	29

TABLE OF CONTENTS

2.2.1	X-Ray Diffraction	29
2.2.2	The Behavior of X-Rays	30
2.2.3	Scanning Electron Microscopy	39
3	Results.....	39
3.1.1	Precursor Method (M1)	40
3.1.2	Sulfate Salt Method (M2)	59
4	Summary and Conclusion.....	64
5	Future Work.....	66

LIST OF FIGURES

Figure 1.1. Atmospheric CO ₂ measurements from ice cores from Law Dome, Antarctica and direct measurement. ²	2
Figure 1.2. Comparison of GHG forcing model to different temperature reconstructions from 1000 to 2000 CE. Heavy dashed line is the temperature prediction using GHG and aerosols. ¹	3
Figure 1.3. Schematic showing the conduction and valence bands of a) metals, b) semiconductors, and c) insulators.	5
Figure 1.4. A simple solar cell consisting of a positively doped material and a negatively doped material. Absorbed light excites electrons into the conduction band and the asymmetry of the electronic properties of the two materials move the electrons into a circuit that can do work.	6
Figure 1.5. A p-i-n cell showing an intrinsic layer between positively charged and negatively charged layers.....	9
Figure 1.6. A bias drop occurs over the intrinsic region of a p-i-n cell.	10
Figure 1.7. Solar cell efficiencies by family of cell. ¹⁶	11
Figure 1.8. Schematic of a dye-sensitized solar cell's basic principles and energy diagram.	13
Figure 1.9. Design of a pyrite sensitized solar cell where pyrite is in contact with WO ₃ , TiO ₂ or ZnO and a contact making a p-i-n heterojunction. ²⁵	15
Figure 1.10. a) Pyrite unit cell showing a dumbbell arrangement of sulfur dimers around lattice points and b) the unit cell of marcasite.	16
Figure 2.1. Iron(III)diethyldithiophosphate is formed from the reaction of iron(III)chloride and diethyldithiol ammonium salt.	21
Figure 2.2. Iron disulfide is formed from the reaction of iron(III)diethyldithiophosphate and hexadecyltrimethylammonium bromide.	22
Figure 2.3. The reaction of iron(II) sulfate, sodium thiosulfate, and elemental sulfur to make cubic pyrite phase iron disulfide.	23
Figure 2.4. Scanning electron micrographs of a), the surface of Au on mica showing grains averaging 50 nm, and b) the surface of Au substrate on Cr wetted silicon showing grains of random shapes ranging in size from 50 nm to 100 nm.	27
Figure 2.5. Unlocked coupled x-ray diffraction of Au on a) Cr wetted Si, b) mica and c) mica from literature.	28
Figure 2.6. Incident angle (blue) in relation to critical angle (red) in three cases: (a) when the critical angle equals the incidence angle, (b) when the critical angle is greater	

TABLE OF CONTENTS

2.2.1	X-Ray Diffraction.....	29
2.2.2	The Behavior of X-Rays.....	30
2.2.3	Scanning Electron Microscopy.....	39
3	Results.....	39
3.1.1	Precursor Method (M1)	40
3.1.2	Sulfate Salt Method (M2).....	59
4	Summary and Conclusion.....	64
5	Future Work.....	66

LIST OF FIGURES

Figure 1.1. Atmospheric CO ₂ measurements from ice cores from Law Dome, Antarctica and direct measurement. ²	2
Figure 1.2. Comparison of GHG forcing model to different temperature reconstructions from 1000 to 2000 CE. Heavy dashed line is the temperature prediction using GHG and aerosols. ¹	3
Figure 1.3. Schematic showing the conduction and valence bands of a) metals, b) semiconductors, and c) insulators.	5
Figure 1.4. A simple solar cell consisting of a positively doped material and a negatively doped material. Absorbed light excites electrons into the conduction band and the asymmetry of the electronic properties of the two materials move the electrons into a circuit that can do work.	6
Figure 1.5. A p-i-n cell showing an intrinsic layer between positively charged and negatively charged layers.....	9
Figure 1.6. A bias drop occurs over the intrinsic region of a p-i-n cell.	10
Figure 1.7. Solar cell efficiencies by family of cell. ¹⁶	11
Figure 1.8. Schematic of a dye-sensitized solar cell's basic principles and energy diagram.	13
Figure 1.9. Design of a pyrite sensitized solar cell where pyrite is in contact with WO ₃ , TiO ₂ or ZnO and a contact making a p-i-n heterojunction. ²⁵	15
Figure 1.10. a) Pyrite unit cell showing a dumbbell arrangement of sulfur dimers around lattice points and b) the unit cell of marcasite.	16
Figure 2.1. Iron(III)diethyldithiophosphate is formed from the reaction of iron(III)chloride and diethyldithiol ammonium salt.	21
Figure 2.2. Iron disulfide is formed from the reaction of iron(III)diethyldithiophosphate and hexadecyltrimethylammonium bromide.	22
Figure 2.3. The reaction of iron(II) sulfate, sodium thiosulfate, and elemental sulfur to make cubic pyrite phase iron disulfide.	23
Figure 2.4. Scanning electron micrographs of a), the surface of Au on mica showing grains averaging 50 nm, and b) the surface of Au substrate on Cr wetted silicon showing grains of random shapes ranging in size from 50 nm to 100 nm.	27
Figure 2.5. Unlocked coupled x-ray diffraction of Au on a) Cr wetted Si, b) mica and c) mica from literature.	28
Figure 2.6. Incident angle (blue) in relation to critical angle (red) in three cases: (a) when the critical angle equals the incidence angle, (b) when the critical angle is greater	

LIST OF FIGURES

than the incidence angle, and (c) when the critical angle is less than the incidence angle.....	31
Figure 2.7. a) Plot of incident radiation angle vs. reflectivity for FeS ₂ , b) first derivative of incident radiation angle vs. reflectivity.	32
Figure 2.8. Photon Energy vs. Attenuation Length for FeS ₂ at 0.5°, 1.0° and 1.5°.....	33
Figure 2.9. Ideal crystal lattice showing satisfaction of the Bragg condition λ shown in yellow.....	35
Figure 2.10. (a) Symmetric scan with moving source and moving detector, (b) symmetric scan with moving specimen and moving detector, (c) asymmetric scan....	38
Figure 2.11. Average of five $2\theta - \omega$ XRD patterns as gathered and having been smoothed by half (0.075), a quarter (0.0375), an eighth (0.01875) as well as just smoothed (0.15).	39
Figure 3.1. Method 1 film synthesized for 4.5 hours at 230 °C using the M1 with a) $\theta - 2\theta$ geometry, b) $\theta - \omega$ geometry, c) grazing incidence geometry and d) a pyrite powder pattern from literature. Yellow vertical lines indicate the expected peaks from the pyrite phase of FeS ₂ with the Miller indices noted at the top. Green dashed lines indicate W L α contamination, pink lines indicate the Au peaks, black dashed lines indicate the copper holder, the green line is likely an FeS species, and the dark blue dashed line is the marcasite (211) reflection at ~52°.....	41
Figure 3.2. X-ray diffraction patterns showing the range between 32.75 2θ and 33.25 2θ by a) locked coupled geometry, b) unlocked coupled geometry, and c) grazing incidence geometry for three different synthesis times with and without CTAB.	47
Figure 3.3. Secondary electron micrographs acquired of M1 films synthesized without CTAB for a) 1.5 hours, b) 3 hours, and c) 4.5 hours. All films had 6 mM of precursor and were synthesized at 230° C.	49
Figure 3.4. Edge view secondary electron micrographs acquired of M1 films synthesized without CTAB for a) 1.5 hours, b) 3 hours, and c) 4.5 hours. All films had 6 mM of precursor and were synthesized at 230° C.	49
Figure 3.5. Secondary electron micrographs acquired of M1 films synthesized with CTAB for a) 1.5 hours, b) 3 hours, and c) 4.5 hours. Films had 5 mM, 5.8 mM and 5.8 mM of precursor respectively, and were synthesized at 230° C.....	50

LIST OF FIGURES

Figure 3.6. Edge view secondary electron micrographs acquired of M1 films synthesized with CTAB for a) 1.5 hours, b) 3 hours, and c) 4.5 hours. Films had 5 mM, 5.8 mM and 5.8 mM of precursor respectively, and were synthesized at 230° C.....	51
Figure 3.7. Secondary electron micrograph acquired of M1 film synthesized with CTAB for 3 hours. Film had 5.8 mM of precursor, and was synthesized at 230° C....	52
Figure 3.8. Film synthesized with 20 mM FeCl ₃ , 35 mM DDAS and 40 mM CTAB at 230 °C for four hours.	52
Figure 3.9. Film synthesized with 20 mM FeCl ₃ , 35 mM DDAS and 20 mM CTAB at 230 °C for four hours.	53
Figure 3.10. Film synthesized with 20 mM FeCl ₃ , 35 mM DDAS and 15 mM CTAB at 230 °C for four hours.	53
Figure 3.11. Film synthesized with 20 mM FeCl ₃ , 35 mM DDAS and 10 mM CTAB at 230 °C for four hours.	53
Figure 3.12. Film synthesized with 20 mM FeCl ₃ , 35 mM DDAS and 0 mM CTAB at 230 °C for four hours.	54
Figure 3.13. GIXRD of films synthesized with 20 mM FeCl ₃ , 35 mM DDAS and 40, 20, 15, 10, and 0 mM CTAB, respectively, at 230 °C for four hours.....	55
Figure 3.14. Two films synthesized with 10 mM FeCl ₃ , 19 mM DDAS and 4 mM CTAB for a 4 hour hold at 230 °C.....	56
Figure 3.17. Two films synthesized with 10 mM FeCl ₃ , 19 mM DDAS and 13 mM CTAB for a 4 hour hold at 230 °C.....	57
Figure 3.18. Films synthesized with 10 mM FeCl ₃ and 19 mM DDAS with a 4 hour hold at 230 °C with CTAB concentrations of a) 5 mM, b) 9 mM and c) 13 mM.	58
Figure 3.19. GIXRD of film synthesized with 10 mM FeCl ₃ , 19 mM DDAS and 5 mM CTAB for a 4 hour hold at 230 °C.	58
Figure 3.20. M2 films synthesized without pH adjustment at a) 150 °C, b) 190 °C, 230 °C.....	59
Figure 3.21. Cross sections of M2 films synthesized without pH adjustment at a) 150 °C, b) 190 °C, 230 °C.	59
Figure 3.22. GIXRD of films synthesized with 20 mM FeSO ₄ and 20 mM Na ₂ S ₂ O ₃ at a)150 °C, b) 190 °C and c) 230 °C with a beginning pH of ~2.	60
Figure 3.23. M2 films synthesized with 33 mM FeSO ₄ and 33 mM Na ₂ S ₂ O ₃ at 250 °C with a) 9 mM NaOH and pH 4.5, b) 14 mM NaOH and pH 6, c) 17 mM NaOH and pH 7.	61

LIST OF FIGURES

Figure 3.24. Cross sections of M2 films synthesized with 33 mM FeSO ₄ and 33 mM Na ₂ S ₂ O ₃ at 250 °C with a) 9 mM NaOH and pH 4.5, b) 14 mM NaOH and pH 6, c) 17 mM NaOH and pH 7.....	61
Figure 3.25. GIXRD of films synthesized at 250 °C with 33 mM FeSO ₄ , 33 Na ₂ S ₂ O ₃ , with a) pH 7, b) pH 6, c) pH 5.	62
Figure 3.26. GIXRD of films synthesized at 250 °C with 33 mM FeSO ₄ , 33 Na ₂ S ₂ O ₃	62
Figure 3.27. a) M1 powder made with 150 mM FeSO ₄ , 150 mM Na ₂ S ₂ O ₃ , at 230 °C for 20 hours, b) M1 film made with 4 mM FeSO ₄ , 3 mM Na ₂ S ₂ O ₃ , at 230 °C for 20 hours, c) M1 film made with 34 mM FeSO ₄ , 34 mM Na ₂ S ₂ O ₃ at 190 °C, d) edge view of preparation shown in c).	63

1 INTRODUCTION

1.1 Fossil Fuels for Energy Generation and Atmospheric CO₂

Energy generation and distribution systems in operation around the world changed dramatically with the industrial revolution of the late eighteenth and early nineteenth centuries, which saw the onset of large scale utilization of fossil fuels. Unprecedented growth followed and brought with it a problem that would not be recognized for over a century: anthropogenic climate change. Combustion of fossil fuels results in the generation of gaseous CO₂, which absorbs energy in the infrared range of the electromagnetic spectrum (700 nm - 1 mm) trapping energy from the sun in the lower atmosphere and increasing the average global temperature. Expanding access to power sources and finding alternatives to the combustion of fossil fuels is a growing problem that will only become more urgent as the population of the earth increases.^{1,2} While CO₂ concentrations have been measured directly recently, CO₂ levels from before 1978 are measured from air trapped in ice. Figure 1.1 shows results of measurements of ice cores from Law Dome, Antarctica.² Three ice cores were extracted from Law Dome that correspond to different periods of time. The CO₂ counts from the ice cores are compared with recent direct atmospheric measurements. Determining atmospheric temperatures is done by analysis of 20th

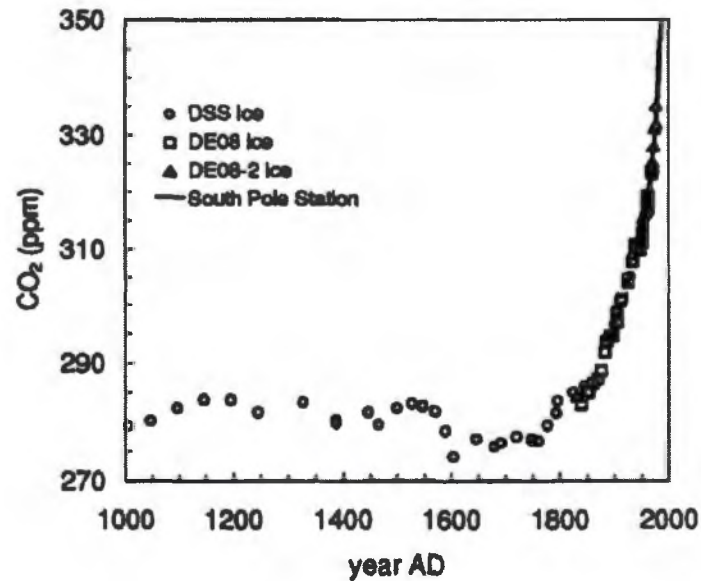


Figure 1.1. Atmospheric CO₂ measurements from ice cores from Law Dome, Antarctica and direct measurement.²

century empirical data of tree rings, corals, and ice cores compared to instrumental data gathered during a period of overlap between 1860 and 1965. Model agreement is robust.¹ Climate reconstruction by ¹⁸O to ¹⁶O ratios, ice layer thickness, pollen in ice cores, sedimentary content and volcanic ash gives data about atmospheric temperature and ocean surface temperature. Climate reconstruction data have been compared with a greenhouse gas (GHG) forcing response model seen in Figure 1.2 that correlates with recorded twentieth century temperature rises. The disagreement between the model and nineteenth century temperatures is explained by the model not regarding the large scale land clearing and albedo changes during that period.¹

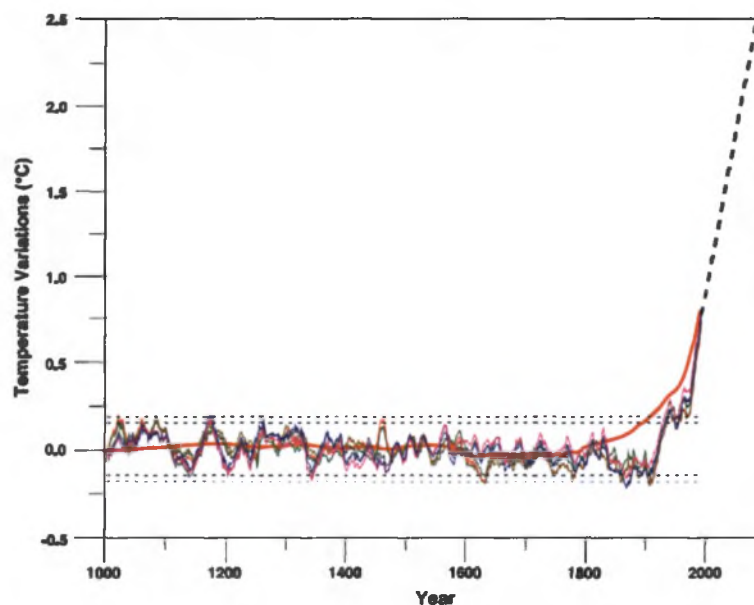


Figure 1.2. Comparison of GHG forcing model to different temperature reconstructions from 1000 to 2000 CE. Heavy dashed line is the temperature prediction using GHG and aerosols.¹

1.2 Atmospheric CO₂ and Climate Change

The increasing concentration of CO₂ (one greenhouse gas) in the earth's atmosphere significantly alters the earth's self-regulating carbon cycle. While it is true that the Earth has seen greater concentrations of CO₂ in the atmosphere in the past, since the appearance of *Homo sapiens* several hundred thousand years ago, the concentration of CO₂ has been relatively stable.³ It is uncertain that our species can survive the large-scale loss of habitat and extinction events that will accompany large scale atmospheric warming. The concentration of atmospheric CO₂ has increased from 280 ppm at the onset of the industrial revolution to 381 ppm as of 2006 and >400 ppm today.⁴ Dissolved CO₂ in the surface waters forms carbonic acid, H₂CO₃, which is

neutralized by the buffering effect of the slightly alkaline surface water. The ocean contributes about half of the removal of atmospheric CO₂. The amount of dissolved CO₂ has increased such that the concentration of hydrogen ions in surface waters has increased by 30%.⁵ The increased concentration cannot be effectively handled by natural carbon sinks such as oceans and sequestration within forests, which are becoming less efficient themselves.⁴ Large scale loss of forested areas from commercial deforestation and, increasingly, wildfires will continue to decrease their efficacy in carbon sequestration. Oceans are becoming warmer and more acidic, which constitutes habitat loss for carbon sequestering organisms such as coccolithophores.⁶ Alternative energy sources such as wind turbines, hydroelectric power and solar cells are attractive options that do not emit greenhouse gasses as a byproduct of energy generation. Transitioning from a dependence on fossil fuels to alternative energy sources will help ameliorate global warming as energy needs increase by an expected factor of two by 2050.⁷ The direct conversion of sunlight to electrical power eliminates the greenhouse gas by products and transfers the need from centralized to localized energy generation and storage.

1.3 Light Induced Charge Separation in Semiconductors

When a semiconducting material absorbs light of sufficient energy that is greater than the band gap, an electron is excited from the valence band into the conduction band, creating an electron-hole pair. If electron-hole charge carriers are

prevented from recombining such that they are able to be separated further by an electric field, then they may enter into an electrical circuit.⁸ Light induced charge separation is shown in Figure 1.4. A semiconductor is a material that has a difference

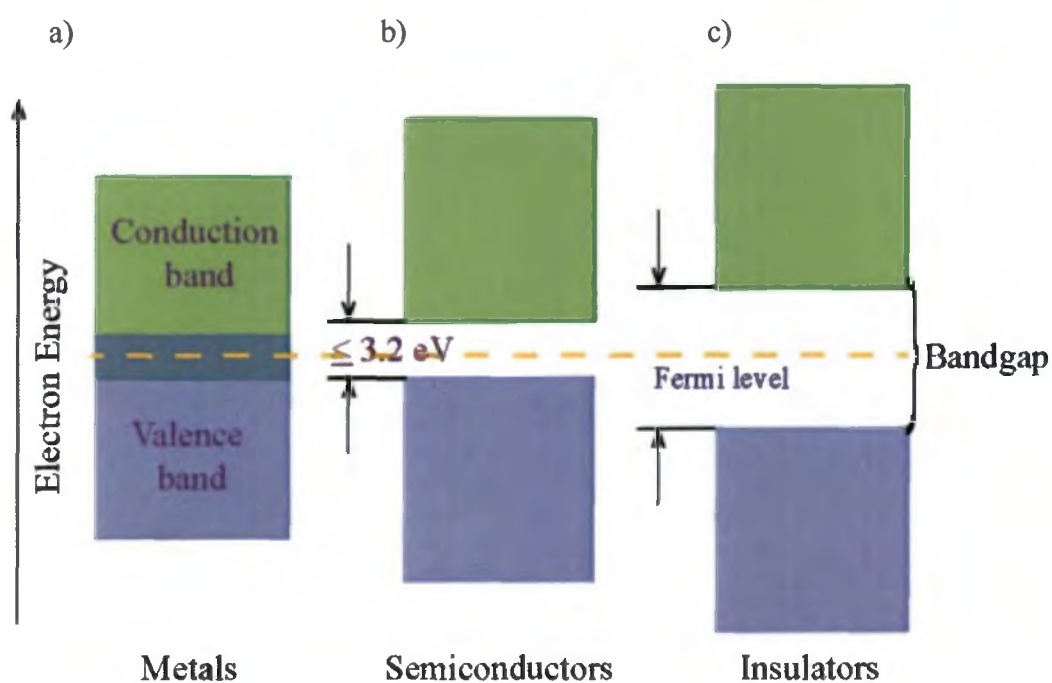


Figure 1.3. Schematic showing the conduction and valence bands of a) metals, b) semiconductors, and c) insulators.

in energy between the filled valence band and the empty conduction band of 0.1 to 3.0 eV ($12.4 \mu\text{m} - 0.4 \mu\text{m}$). Figure 1.4 is a schematic of a simple solar cell consisting of a positively doped material and a negatively doped material in contact. Absorbed light excites electrons from the valence band into the conduction band. The asymmetry of electrical properties of the two materials move- the electrons into a circuit where they can do work.

Examining all different kinds of semiconductors that absorb at various wavelengths for their application in different types of solar cells will increase the variety of applications we can employ them in and the areas of the electromagnetic spectrum we can take advantage of.

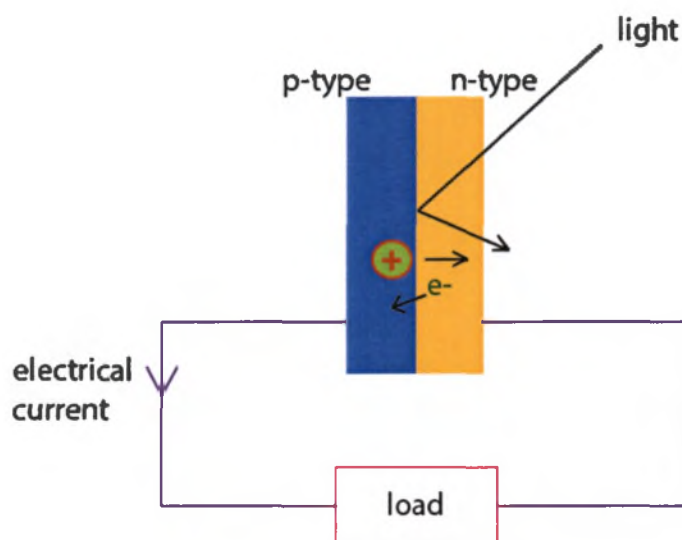


Figure 1.4. A simple solar cell consisting of a positively doped material and a negatively doped material. Absorbed light excites electrons into the conduction band and the asymmetry of the electronic properties of the two materials move the electrons into a circuit that can do work.

1.4 Solar Cells

The need for renewable energy incites interest in new materials for solar or photovoltaic cells. Solar cells that are flexible, made from conducting polymers, use novel absorbers and made from abundant non-toxic elements for electron transport are all active areas of research, as well as investigations into materials made from more

abundant elements.⁹ Of special interest are PV cells made from abundant elements that are easily processed since one of the largest costs in the manufacture of silicon based PVs is the cost to isolate and purify silicon. Over one million metric tons of silicon are refined each year at a cost of 11-13 MWh/ton.¹⁰

1.4.1 Single Crystal Light Absorber

There are a variety of solar cells produced today, each with specific advantages and drawbacks. Silicon is the material that dominates the market, and it is utilized in several types of cell. Single crystal silicon solar cells have an efficiency of around 20%, provide excellent carrier mobility and are readily doped with boron or phosphorous to produce positively doped (p-type) and negatively doped (n-type) silicon, respectively.¹¹ Single-crystal silicon solar cells have been in use for decades and have been invaluable providing power along with GaAs solar cells for space exploration. The manufacture of pure silicon is costly. Boules of single crystals are pulled slowly from molten silicon, directed by seed crystals. Both single-crystal and polycrystalline silicon have been used to fabricate solar cells. To date, the highest reported efficiencies for the conversion of sunlight to electrical energy for single-crystal and polycrystalline silicon solar cells are 24.4% (Sun Power) and 19.2% (Mitsubishi Electric). While polycrystalline Si solar cells are have an efficiency of 12 – 15 % single-crystal Si solar cells, the cost of manufacturing poly-crystalline solar

cells is lower than that of single-crystal solar cells, increasing their attractiveness for use on the surface of the Earth.^{8,12}

1.4.1 Polycrystalline Silicon (p-Si)

In the fabrication of polycrystalline Si solar cells, the molten silicon is cast into blocks of polycrystalline material with domains of random size, shape and orientation. Efficiency is lowered by defects at the grain boundaries that reduce charge carrier mobility and facilitate electron-hole recombination. The casting process enables the manufacture of square and rectangular cells, utilizing space better than the truncated squares that are made from the naturally cylindrical single crystalline silicon boules wafers.

1.4.2 Amorphous Silicon (a-Si)

Since the 1980's small amorphous silicon cells have been used to power watches, calculators and other small items that require a very small amount of power to operate. The low efficiency of these cells ~7-8% (less than half that of single crystal cells) is adequate for these small scale applications but is not economically feasible for large power generation applications.¹¹ The discovery that the addition of hydrogen to amorphous silicon passivates dangling bonds in the material, reducing charge carrier recombination, has prompted its use as an intrinsic layer in a p-doped, intrinsic, n-doped (p-i-n) cell.¹³ Undoped materials that increase the distance charge carriers travel

toward a charged region are intrinsic. The exposure of H-passivated a-Si to sunlight causes the defect density to increase (Wronski effect) such that the efficiency of these cells decreases over time by as much as 35% to an efficiency as low as 4%.¹⁴ The

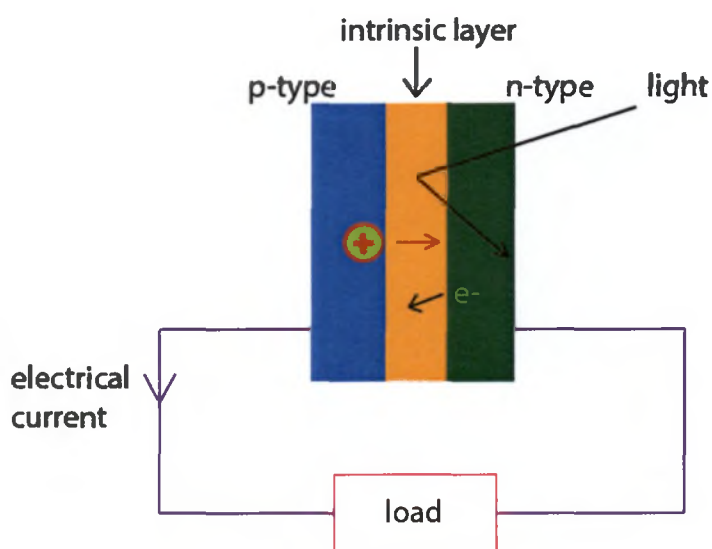


Figure 1.5. A p-i-n cell showing an intrinsic layer between positively charged and negatively charged layers.

addition of an intrinsic layer increases the thickness of the region in which photons are absorbed. The built-in bias drops over the intrinsic region, as seen in Figure 1.6, creating an electric field that drives charge separation with e^- going toward the p-region. Typical thickness of silicon based PV are 300 microns for single crystalline, polycrystalline, and a-Si PV cells.¹⁵ This is due to the fact that silicon is relatively inefficient absorber of vis-NIR light. Its bandgap is

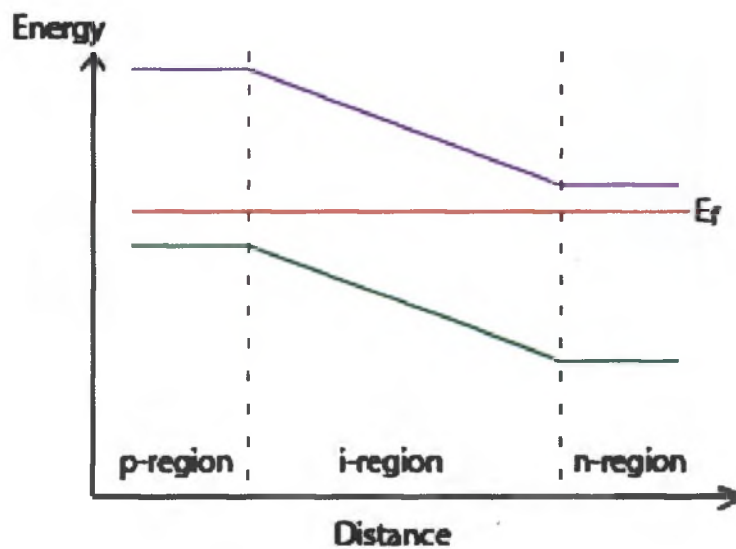


Figure 1.6. A bias drop occurs over the intrinsic region of a p-i-n cell.

Table 1.1. Energy and band gap for various materials.¹⁴

Material	E_g (eV)	Band Gap	Efficiency
Si	1.11	indirect	25.0 ± 0.5
Si-p			20.4 ± 0.5
CdTe	1.44	direct	16.7 ± 0.5
GaAs	1.4	direct	27.6 ± 0.8
TiO ₂ (anatase)	3.2	indirect	
FeS ₂	0.95	indirect	
GaInP/GaAs/Ge			32.0 ± 1.5

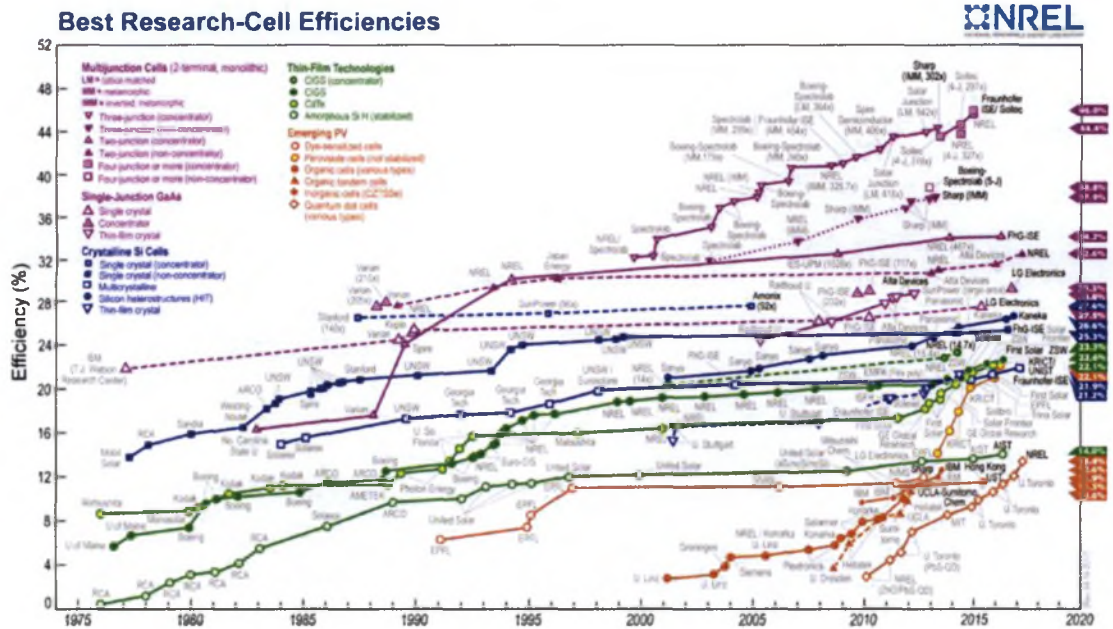


Figure 1.7. Solar cell efficiencies by family of cell.¹⁶

1.5 Semiconducting Thin Films

An alternative to Si is to employ semiconducting thin films in which the absorber has a large absorption coefficient. Thin films have also allowed the expansion of available materials for use in solar cells. For example, copper indium diselenide (CIS) cells are used in layered heterojunction cells with a cadmium sulfide layer and gold or molybdenum metal backings. CIS cells are dark grey or black and can be made semitransparent, garnering favor with architects for their ability to be integrated into buildings in an aesthetic manner. However, indium is rare in the Earth's crust, and is in demand for other electronic applications. More importantly, cadmium is a cumulative toxin making the manufacture and eventual decommissioning of these cells problematic.

1.5.1 Cadmium Telluride Cells

Cadmium telluride (CdTe) has an advantage over CIS cells in that cadmium is less toxic when combined with tellurium, both of these elements are more abundant than indium. Cadmium telluride solar cells are the simplest and least expensive to manufacture of the thin film cells. They have short energy payback times and since cadmium is a byproduct of the zinc mining industry, the manufacture and use of CdTe solar cells help to mitigate an existing problem.¹⁷

1.5.2 Gallium Arsenide Cells

Gallium arsenide (GaAs) is the archetypal III-V semiconductor and has higher efficiencies (~30%) than other thin films.¹⁸ Gallium arsenide is less susceptible to radiation damage than silicon, and is thus an excellent choice for use in space and for solar concentration applications. InGaP/InGaAs/Ge triple junction solar cells with an efficiency of 28.7% are now employed to power spacecraft.¹⁹ However, GaAs is very expensive and its utilization is limited to applications that demand high efficiency and reliability such as providing solar power for remote-controlled missions on the surface of Mars.¹⁷

1.5.3 Dye Sensitized Cells

A novel development are dye sensitized solar cells (DSSC), which are a mixed organic/inorganic solar cell that typically combines titanium dioxide (TiO_2), organic dye, and an electrolyte to make a third generation solar cell. In DSSCs, a transparent mechanical support covered with a transparent conductive oxide (TCO) is next to the light absorber, a ruthenium based dye bonded to TiO_2 nanoparticles, which serves as the charge carrier-transport layer.²⁰ As seen in Figure 1.8 the dye absorbs light and injects electrons into the conduction band of the TiO_2 semiconductor. The electron moves through the semiconductor to the back contact (TCO), through the load, and then to the counter electrode, often platinum, where it reduces the redox mediator, I_2/I_3^- , thereby regenerating the sensitizer.²¹ The dye is oxidized during this electron transfer process. No electron-hole pairs exist in the semiconductor, making the system analogous to a leaf, where chlorophyll is the injector.²² DSSC's work very

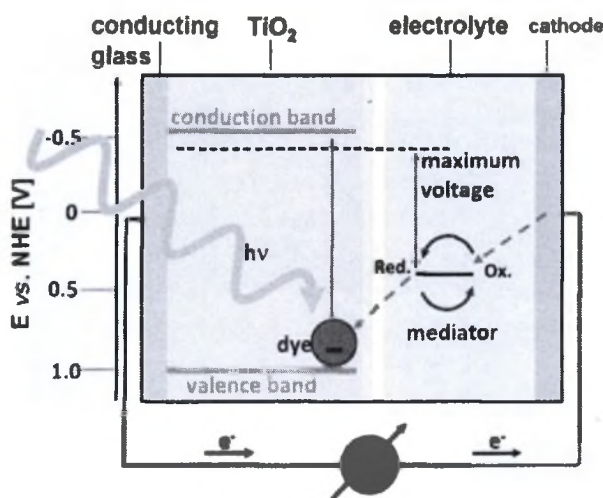


Figure 1.8. Schematic of a dye-sensitized solar cell's basic principles and energy diagram.

well in low and diffuse light, at high ambient temperatures, and are nontoxic (except for the fluid phase containing acetonitrile), with a fast roll to roll manufacturing time. The efficiencies of DSSCs depend on the kinetics of the electron transfer process and relative energy levels and the junction of the liquid and the solid. The rate of electron injection must be faster than the dye's excited state decay time.²³ The ability of DSSCs to work well under low light intensity/conditions make them attractive for use in areas without a significant percentage of strong daily sunlight, as well as for incorporation into a wide range of building components.¹¹

1.6 The Case for FeS₂ Absorbers

The pyrite phase of FeS₂ has attracted interest to serve as an absorbing layer for a solar cell because of its low band gap of 0.95 eV and thus its ability to absorb energy in the visible and near-infrared regions of the electromagnetic spectrum. Pyrite has an indirect band gap of 0.95 eV, and its high absorption coefficient, ($\alpha \times 10^5 \text{ cm}^{-1}$ at 633 nm), enables a film of just 10 nm to absorb 90% of the incident light.^{24,25} In addition, both Fe and S are abundant and nontoxic elements in the Earth's crust. When surface roughness of a material is of the same order as the wavelength of the incident light, strong scattering occurs which greatly reduces the percentage of incident light entering the material. Pyrite films that can be formed with extremely smooth surfaces,

which combined with its large absorption coefficient, make an attractive material for solar cells.

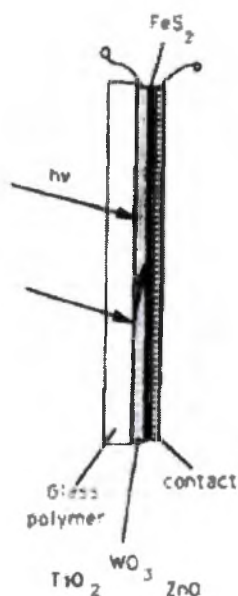


Figure 1.9. Design of a pyrite sensitized solar cell where pyrite is in contact with WO_3 , TiO_2 or ZnO and a contact making a p-i-n heterojunction.²⁵

Pyrite could find use as an electron injector when placed in contact with a wide band gap semiconductor such as titanium dioxide (TiO_2) similar to the way organic dyes improve the efficiency of DSSC's.²⁵ The resulting p-i-n heterojunction solar cell would not suffer the problems inherent that the limited stability of the organic dyes and technical difficulties that liquid contacts bring to DSSC's.

The most stable mineral phase of the iron sulfides (Fe_xS_y) is pyrite, FeS_2 ,

Figure 1.10 a. Pyrite is a stable semiconductor with a bandgap of 0.95 eV,

corresponding to a wavelength of $1.31 \mu\text{m}$.²⁵ Marcasite is another mineral phase with

the FeS_2 stoichiometry. Marcasite is a metastable orthorhombic semiconductor with a bandgap of (0.32) eV which corresponds to a 3.87 μm wavelength of light. Marcasite oxidizes readily and its unit cell is shown in Figure 1.10 b.

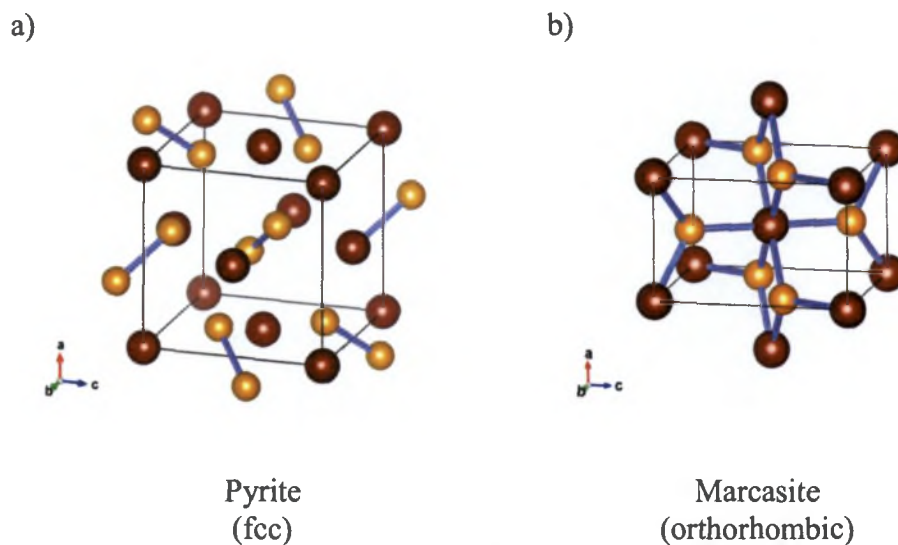


Figure 1.10. a) Pyrite unit cell showing a dumbbell arrangement of sulfur dimers around lattice points and b) the unit cell of marcasite.

1.6.1 Synthesis of Iron Sulfides

Iron sulfides grown by geothermal routes are well known from research involved in the geological sulfur cycle, but little research has been performed on hydrothermally synthesized iron sulfides in the laboratory.²⁶ A method that consistently results in a thin smooth film of pyrite phase iron disulfide would be desirable as an absorber in a heterojunction solar cell.

1.6.2 Metal-Organic Chemical Vapor Deposition

Thin films of pyrite have been synthesized by several methods. The earliest method of pyrite film formation employed metal-organic chemical vapor deposition (MOCVD). The MOCVD method employs an organic carrier molecule with a metal ligand in a pressure-controlled system at high temperatures ($\sim 450^\circ\text{C}$) to bring the reagents into contact with a hot substrate where the desired material is formed by chemical reaction. The carrier gas is a nonreactive gas such as Ar, and the partial pressure of each reagent-carrying gas is controlled to optimize the stoichiometry of the desired crystalline phase. The as-deposited films of FeS_2 have large crystallites with low root mean square (rms) roughness. However, the gas-phase reagents do not always bond with the substrate and there is a high likelihood of secondary products being produced and incorporated into the bulk of the film.²⁷

1.6.1 Sulfurization of Iron

The sulfurization of Fe^0 films is also used to grow FeS_2 films. There are two ways in which this can be accomplished; a hydrothermal method and a gas phase method.^{28,29} The hydrothermal method employs a thin Fe foil and elemental S in water or hydrazine in a Teflon-lined autoclave at moderate temperatures ($\sim 150^\circ\text{C}$) for typical durations ranging from 12 to 24 hours. The S diffuses into the Fe and an iron FeS film forms at the surface. The solvent is used to selectively control the phase and stoichiometry of the resulting film. The solvent technique uses considerably more iron

than the end product requires since it is used as the support for the reaction and the presence of excess iron limits the applications for which the prepared film can be used.²⁹ Films prepared by the hydrothermal method are rough, making them unsuitable for use as an electron injector in a semiconducting heterojunction PV cell because the light is scattered at the surface of the film reducing the fraction of light entering the film.

The gas phase technique of iron pyrite formation starts with a thin film of Fe deposited by vapor deposition onto a non-conducting substrate. The substrate and film are sealed under Ar in an ampule filled with sufficient elemental sulfur to achieve the desired partial pressure of sulfur at the reaction temperature, and at a pressure of approximately 80 kPa. The reaction is carried out at 673 K for approximately 20 hours. The resulting films are comprised of submicron-sized crystallites, have a non-uniform thickness of 70 to 600 nm when starting from films ranging from 25 to 150 nm. X-ray diffraction shows FeS₂ peaks for all films, with unidentified peaks adjacent to the (200) peak and lower intensities in the thinnest films.²⁹

1.6.2 Hot Injection

Another technique is to synthesize nanocrystals by hot injection and sinter them onto a substrate to form a thin film.²⁹ Typically a solvent and a reagent are reacted to form a molecular iron precursor in solution at around 150°C. Reagents introduced into the system rapidly react at a critical temperature, between 15 s to 90 s,

before burst nucleation occurs after which there is a rapid decrease in the concentration of monomers.³⁰ Hot sulfur stock in solvent is then injected into the system and the reaction typically takes place during a 2 hour period. Nucleation is fast and uniform, producing stable, pure pyrite phase nanocrystals of uniform size. Particle size depends on the temperature of the system and when the reaction is quenched. The nanocrystals are then sintered onto substrates to form a mechanically stable film. Films synthesized by hot injection can have large voids ranging from tens of nanometers to a micron between crystallites and the process involves multiple steps where problems can occur.^{31,32}

1.7 Low Temperature Synthesis and Research Goals

1.7.1 The Advantage of Hydrothermal Synthetic Methods

A one-step hydrothermal synthetic route is attractive because of its simplicity. There is no need to maintain a vacuum or for gas handling or high temperature solid state reaction equipment. One of the simplest methods to grow the pyrite phase in a single step is based on hydrothermal synthesis. In a typical hydrothermal reaction, starting reagents of the target inorganic phase are dissolved or mixed with water and introduced into a Teflon liner, which is sealed in a stainless steel reactor. The reactor is placed in an oven at relatively low temperatures compared to MOCVD, ~150- 250 °C,

for up to 24 hours. Using hydrothermal conditions and different precursors Wu et al.³³ and Wadia et al.³⁴ found that pyrite nanocrystals could be prepared.

In this work, two literature methods for preparing pyrite nanoparticles were adapted to the synthesis of films. The first method (M1) employs an iron-centered organometallic precursor that is prepared in advance or in situ and then decomposed hydrothermally to produce pyrite. The second method (M2) is a simple one-step synthesis starting from FeSO₄, sodium thiosulfate (Na₂S₂O₃), and extra sulfur to drive the reaction toward stoichiometric FeS₂.

1.7.2 Research Goals

In the research presented here, the goal was to develop a quick, efficient, low temperature hydrothermal method of producing smooth thin films of pyrite phase FeS₂ for use as a light absorbing layer in a heterojunction solar cell. Two methods will be explored, one that employs Fe³⁺ (M1) and another with Fe²⁺ (M2) as precursor iron sources species in solution with the goal of achieving a thin film of the thermodynamically stable pyrite phase FeS₂. In addition, the effects of the temperature, synthesis time, and reagent concentration were tested for their effect on the amount of pyrite phase formed and the resulting film thickness. The primary characterization methods are X-ray diffraction and scanning electron microscopy, which are used to unambiguously identify the phase(s) present and the film and crystallite morphology, respectively.

2 EXPERIMENTAL METHODS

2.1 Materials Synthesis

In this section, the synthesis procedure for preparing FeS₂ thin films will be described in detail. This will be followed by a description of the methods that were used to characterize the films. The analysis methods and any software will be summarized.

2.1.1 Precursor Method (M1)

The first method of pyrite film synthesis was adapted from the work of Wadia et al. Wadia et al that focused on the preparation of nanocrystalline FeS₂.³⁴ In this method, an organometallic precursor was synthesized that was then hydrothermally decomposed in the presence of the surfactant hexadecyltrimethylammonium bromide (CTAB) to prepare FeS₂ nanocrystals, Figure 2.1 and Figure 2.2.

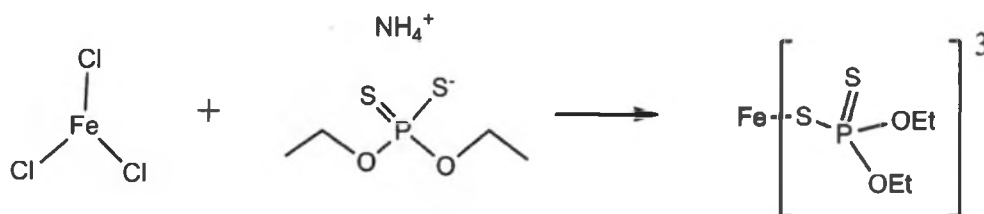


Figure 2.1. Iron(III)diethyldithiophosphate is formed from the reaction of iron(III)chloride and diethyldithiol ammonium salt.

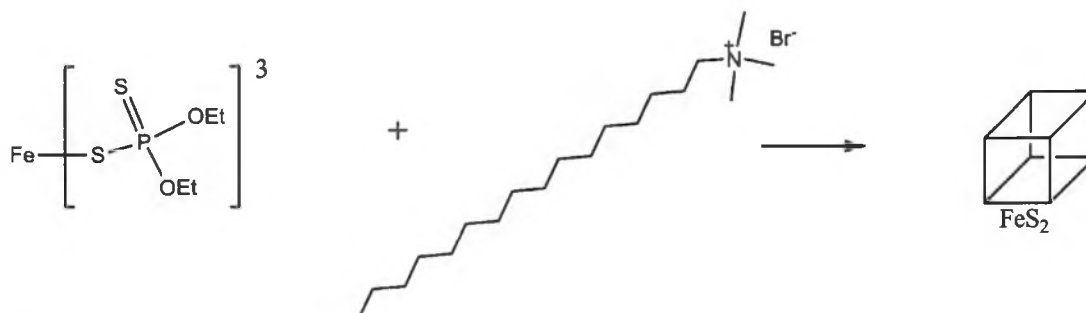


Figure 2.2. Iron disulfide is formed from the reaction of iron(III)diethyldithiophosphate and hexadecyltrimethylammonium bromide.

The precursor was prepared from iron(III)chloride (FeCl_3) and diethyldithiol ammonium salt (DDAS), forming iron(III)diethyldithiophosphate, a solid precursor. The precursor and the surfactant CTAB were varied in concentration to optimize synthesis conditions. The synthesis of FeS_2 by the precursor method was approached two ways. In the first method, the precipitate formed by the reaction of DDAS and FeCl_3 was collected and dried under vacuum for 24 hours before adding a known quantity to a solution of CTAB. The precursor is extremely hygroscopic, adding an amount of error to the yield measurements. Powder collected from syntheses without substrate indicate 1000 % yield, an impossibility. The concentration of solid precursor ranged from 3 mM to 13 mM, and the CTAB concentration ranged from 0 mM to 6.6 mM.

In the second variation, solutions of FeCl_3 , DDAS and CTAB were added to the reaction chamber together immediately prior to heating. The second approach was explored since a precipitate was formed immediately on mixing FeCl_3 and DDAS.

Synthesis reaction times ranged between 1 and 6 hours. Concentration of FeCl_3 ranged from 8 mM to 18 mM, concentration of DDAS ranged from 10 mM to 67 mM, and the concentration of CTAB ranged from 0 mM to 179 mM. The temperature ranged between 150 °C and 230 °C.

Another synthesis variation included soaking the evaporated gold on silicon substrate in a CTAB solution, rinsing with deionized water, and drying before placing the substrate in reaction vessel and adding solutions of FeCl_3 and DDAS.

2.1.2 Sulfate Salt Method (M2)

The second method used iron(II)sulfate (FeSO_4), sodium thiosulfate ($\text{Na}_2\text{S}_2\text{O}_3$), and elemental sulfur (S), in a single step hydrothermal method. Concentration of FeSO_4 ranged from 10 mM to 159 mM, concentration of $\text{Na}_2\text{S}_2\text{O}_3$ ranged from 10 mM to 150 mM, and the concentration of elemental sulfur ranged from 0.3 mM to 0.7 mM. For some syntheses in M2, 0.1 M NaOH was added dropwise to the reaction vessel to raise the pH of the starting solution to drive the formation of the pyrite phase. Starting

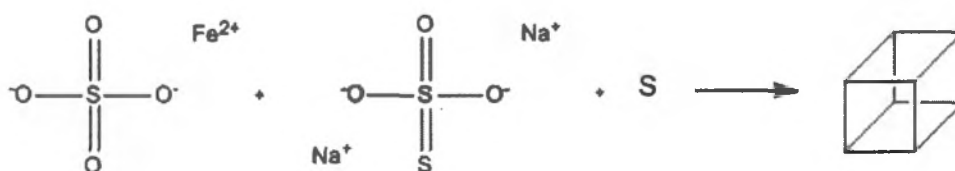


Figure 2.3. The reaction of iron(II) sulfate, sodium thiosulfate, and elemental sulfur to make cubic pyrite phase iron disulfide.

pH was close to 3.3 for syntheses without pH adjustment and ranged from 4.45 to 6.23 with added NaOH. When the pH approached 6 a green precipitate formed and the pH stopped increasing. Temperature ranged from 150 °C to 250 °C.

2.1.3 Preparation of Substrate

2.1.3.1 Silicon wafers

Single side polished prime grade silicon wafers with (100) orientation were cleaned with basic piranha standard clean (SC-1) from the first step of the Radio Corporation of America (RCA) cleaning procedure, rinsed with copious deionized water and followed by 100% ethanol, and immediately dried under a stream of argon gas. The SC-1 solution was prepared in clean glass vessels in a hood from one part NH_4OH (29%), one part H_2O_2 (30%) and five parts water. The water and NH_4OH were heated to above 70 °C before the addition of the H_2O_2 . The SC-1 solution is allowed to react for one minute before the Si wafers were added. Wafers were soaked in the piranha solution for ten minutes before rinsing with deionized water and 100% ethanol and drying with Ar.

The cleaned wafers were then placed directly inside the bell jar of a Veeco vacuum chamber and evacuated to a pressure of 1.7×10^{-7} Torr. Cr plated W rods and Au (99.99% purity; ~150-300 mg) from Lesker were loaded onto a W boat from R. D. Mathis were used for deposition. The overall process of metal evaporation consists of

several steps: 1) removal of oxide and contaminants from the Cr and Au, respectively; 2) bake-out of the vacuum chamber to reduce the pressure to $\leq 10^{-7}$ Torr by removing adsorbed water and gases from the chamber walls and substrate; and 3) heating the metals sequentially to their sublimation and evaporation temperatures for Cr and Au, respectively.

First, the natural chromium oxide was removed from the source metal by heating the Cr-coated W rod with a current of 50 Amperes for sufficient time to bring the pressure up to 2×10^{-6} Torr. Then, the pressure began to fall as the more volatile oxide was removed, at which point the current to the Cr was turned off. Next, a W boat containing the Au pellets was heated with a current of 60 Amperes until the gold melted, then the current was lowered to 50 Amperes for five hours to radiatively heat the chamber. This heating step or “bakeout” removed adsorbed gasses from the vacuum chamber surfaces. Finally, Cr was sublimed and Au was evaporated at maximum rates of 0.5 nm/s and 1 nm/s, respectively, to achieve layers of 5 nm of Cr and 150 nm of Au. After the gold evaporation step, the vacuum chamber was vented with filtered Ar gas and the substrate removed and stored in Nalgene wafer holders. The Au surface was found to have a predominately (111) texture on both Si and mica. The average grain size of 50 nm in size on mica and have a consistently round shape while the grains on Si have randomly shaped grains ranging in size from 50 nm to 100 nm.

2.1.3.2 Mica Substrate

Muscovite ($\text{H}_2\text{KAl}_3(\text{SiO}_4)_3$) mica cleaves parallel to the basal plane to give an atomically smooth surface that is ideal for thin film deposition. There is no need for a Cr wetting layer if Au is thermally evaporated onto mica. However, the mica must be heated to desorb any adsorbed molecules on the surface, but not so much as to start dihydroxylation from the interior of the mineral, which would result in an unsuitable substrate.³⁵ A substrate holder equipped with a thermocouple and two rod shaped heating elements mounted in a steel block was fabricated in-house for this purpose. Muscovite mica (1" disks from Russia) substrate was prepared for the bell jar by cleaving with a clean surgical steel razor immediately before being mounted on the substrate heater and introduced into the bell jar. A bakeout was performed by heating a W boat containing gold pellets with a current of 60 amperes until the Au melted, then the current was lowered to 50 Amperes for five h to radiatively heat the chamber, thereby desorbing adsorbed gasses from the vacuum chamber surfaces. After the chamber bakeout, the substrate heater was heated to 250 °C and Au evaporated at 35 Å/s until 100 nm had been deposited and then slowed to 1.5 Å/s until a final thickness of 200 nm had been deposited. The temperature of the wafers was increased over an hour to 450 °C, and then held for two hours at 450 °C before cooling to room temperature overnight, venting with filtered argon gas and removing from the bell jar.

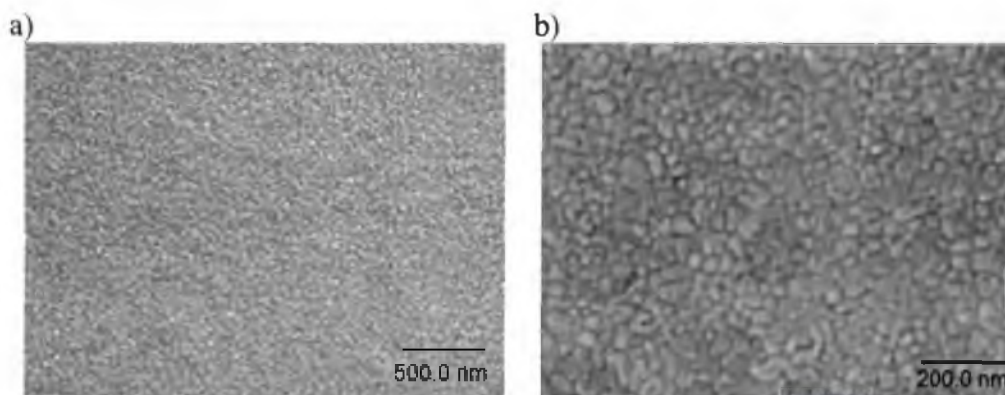


Figure 2.4. Scanning electron micrographs of a), the surface of Au on mica showing grains averaging 50 nm, and b) the surface of Au substrate on Cr wetted silicon showing grains of random shapes ranging in size from 50 nm to 100 nm.

X-ray diffraction (Figure 2.5) of the deposited gold shows a strong (111) orientation for both the mica and the Cr wetted Si, with a peak at $38.23^\circ 2\theta$. Other Au peaks are not observed. There are spurious peaks in the scans of both the mica and the Cr wetted Si from a misaligned goniometer, and the mica pattern contains basal plane reflections of the mica.

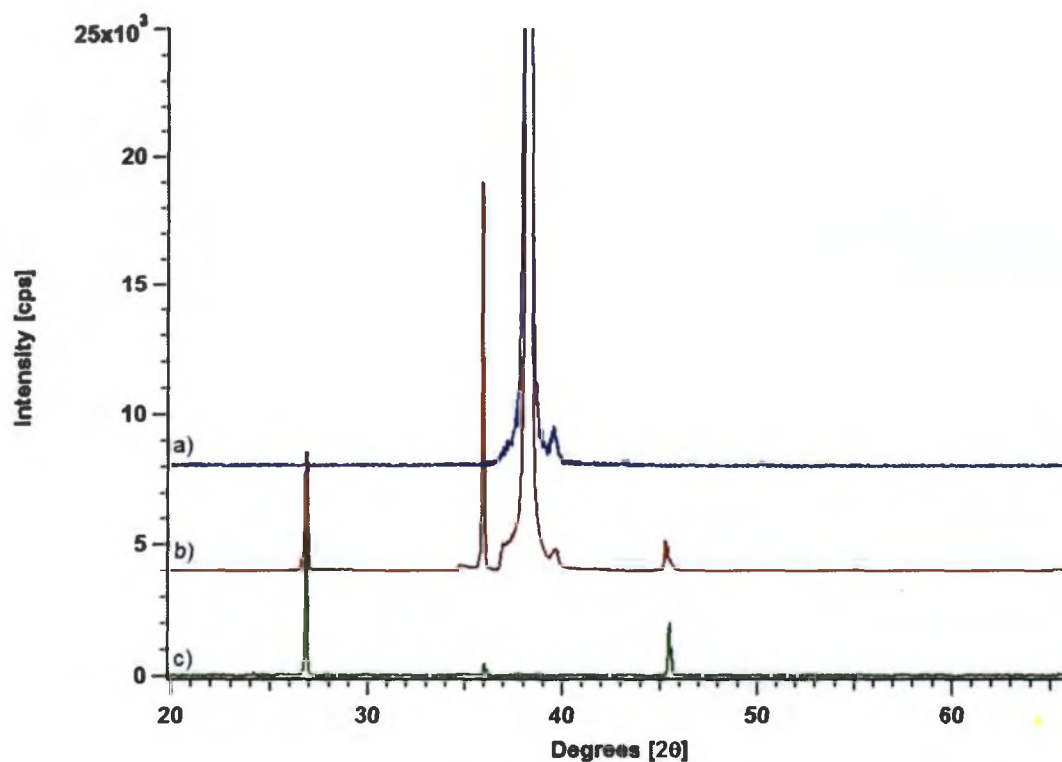


Figure 2.5. Unlocked coupled x-ray diffraction of Au on a) Cr wetted Si, b) mica and c) mica from literature.

2.1.3.3 Preparation of Films and Powders.

A Parr acid digestion reaction vessel was utilized in the hydrothermal synthesis of pyrite phase films and powders. Two Au coated substrates were placed upright in Teflon liners on Teflon holders with the gold surfaces facing away from the center and sealed with all reagents in a Parr acid digestion reaction vessel. Precipitates (are they any precipitates available for XRD? From one of the precursor high temp syntheses?) were filtered and washed successively with deionized water, carbon disulfide (CS_2), dilute acid (1 mM HCl) and rinsed profusely with deionized water. The powders were then dried for 4 hours at 60 °C and the films dried under a steam of Ar.

2.1.3.4 Teflon Liner Cleaning.

As a result of the pyrite synthesis, the Teflon liners were stained by the iron sulfides formed. The Teflon liners were cleaned between synthesis runs by filling 2/3 of the reactor with dilute (1 mM) HCl, sealing and heating to 180 °C in a Parr reaction vessel for 10 to 12 hours. After cooling to room temperature, the acid was removed, replaced with deionized water and heated to 230 °C for 24 hours. The deionized water treatment was repeated twice.

2.2 Materials Characterization

2.2.1 X-Ray Diffraction

X-ray diffraction (XRD) was carried out using a Bruker D8 Advance powder diffractometer employing a copper anode ($K\alpha$, $\lambda = 1.5406 \text{ \AA}$) with cathode energy of 40 kV and 40 mA. Grazing incidence X-ray diffraction (GIXRD) patterns were acquired at increments of 0.02 degrees 2θ at 3 seconds per step between $20 - 60^\circ 2\theta$ at an incident angle of 1° . Each film was aligned such that the film surface was parallel to the X-ray beam and blocked 50% of the beam before setting the grazing incidence angle. The position of the apex of the rocking curve was used to adjust the drive position of theta in each scan to ensure an incidence angle of 1° . A custom designed accessory to hold and align wafers was manufactured in-house. Unlocked coupled X-

ray diffraction ($2\theta - \omega$) scans were performed to obtain diffraction patterns from the bulk of the films. The diffracted radiation was collected through a thin film slit assembly employing a NaI scintillation counter.

To determine the peak positions and integrated areas, the diffractions patterns were fit with Igor Pro's Multiplex Fitting 2 algorithm. For each diffraction pattern, the dependent variables were peak position, amplitude, and FWHM. From the amplitude and FWHM, the area (integrated intensity) of each peak was determined.

2.2.2 The Behavior of X-Rays

The behavior of X-rays when they interact with a crystalline solid depends on the incident angle and the density of the material. In this discussion, the sample is assumed to be perfectly smooth. In the absence of absorption effects, light incident on a surface may be reflected or transmitted through the sample depending on the angle of incidence. When the X-ray beam is at an angle, α , less than the critical angle, θ_c , the X-rays are reflected from the smooth surface. When $\alpha > \theta_c$, light is transmitted into the specimen at an angle that depends on the material's refractive index with an incident angle that is less than the critical angle. The refraction phenomenon is familiar in optics with the behavior of light at the interface between air and water. A beam of light passing through the water toward the surface at or below its critical angle reflects back into the water. For X-rays, the index of refraction and critical angle depends on the atomic composition and density of the material through the mass

absorption coefficient, μ . In Figure 2.6 a, the critical angle is equal to the angle of incidence, shown in red. In this case, some X-rays are reflected away from the surface and some are propagated along the surface in an evanescent wave. In Figure 2.6 b, the angle of incidence, shown in blue, is less than the critical angle, and

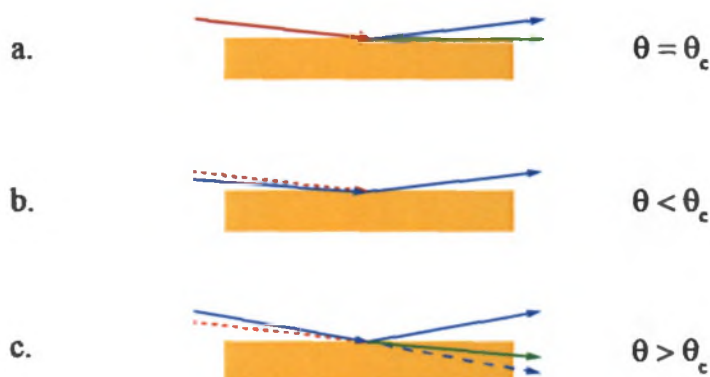


Figure 2.6. Incident angle (blue) in relation to critical angle (red) in three cases: (a) when the critical angle equals the incidence angle, (b) when the critical angle is greater than the incidence angle, and (c) when the critical angle is less than the incidence angle.

all of the X-rays are externally reflected. In Figure 2.6 c, where the angle of incidence is greater than the critical angle, there is penetration of X-rays into the material. In the case of the pyrite phase FeS_2 , the refractive index is less than one, so the radiation travels along a path that traces an angle that is less than the incident angle, shown in green. In Figure 2.7 the plot of incident angle vs. reflectivity is shown. Reflectivity is the ratio

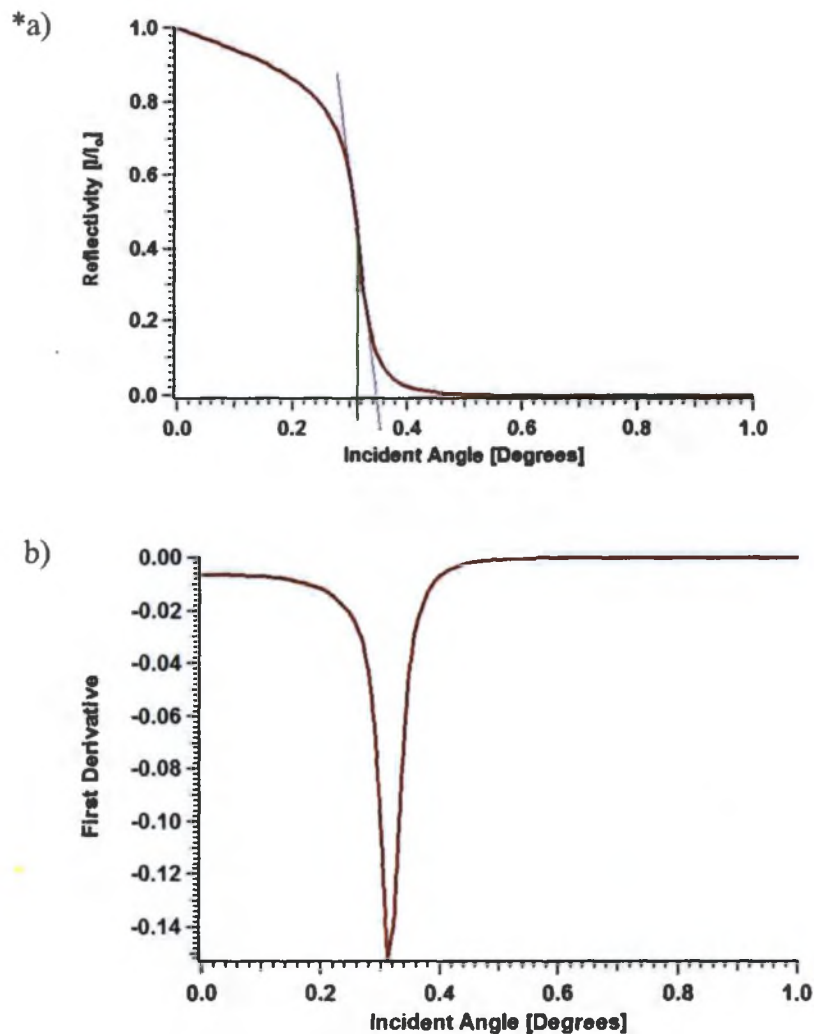


Figure 2.7. a) Plot of incident radiation angle vs. reflectivity for FeS₂, b) first derivative of incident radiation angle vs. reflectivity.

of reflected radiation to incident radiation, and the inflection point (the cusp of the first derivative) of the graph is defined as the critical point (Figure 2.7 b). For an FeS₂ film that is 900 nm thick with a rms roughness of 2 nm and a density of 4.9 g/cm³, the critical angle is 0.31° when the incident beam has an energy of 8.05 keV, as is the case with Cu K_α radiation. The distance that the X-rays travel into a film is estimated by

tracing a line from the plot of photon energy vs. attenuation length from the point on the abscissa that equals the beam energy to the ordinate, which shows attenuation length. Figure 2.8 shows the attenuation length of Cu K_{α} radiation for FeS₂ at three

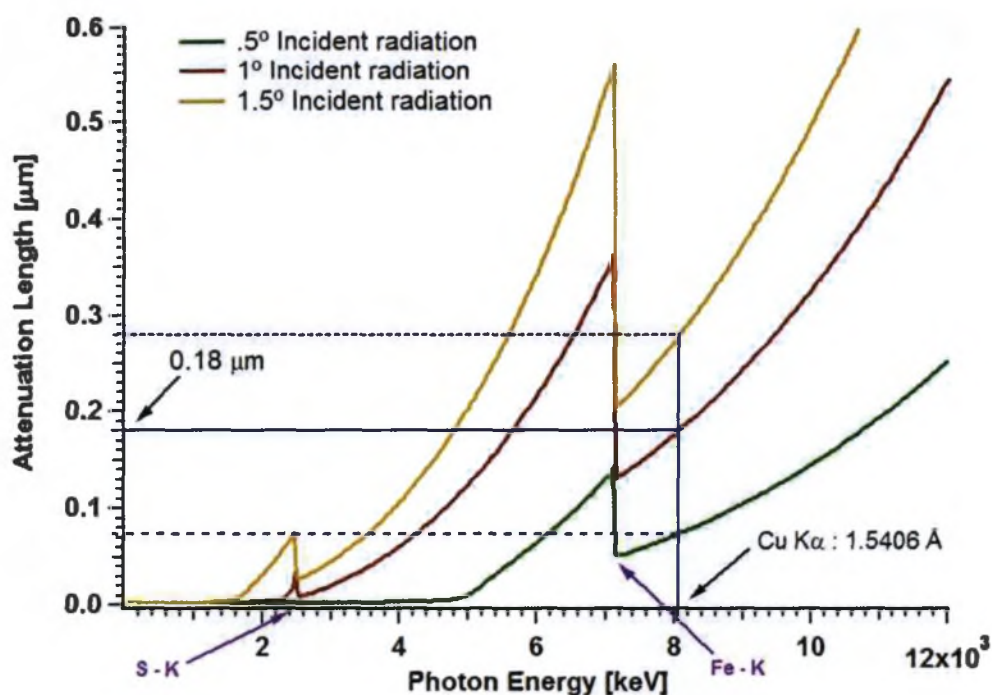


Figure 2.8. Photon Energy vs. Attenuation Length for FeS₂ at 0.5°, 1.0° and 1.5°.

angles, 0.5°, 1° and 1.5°. Just above 2.4 keV is the absorption edge of sulfur's K shell. The K-shell edge of Fe occurs at 7.1 keV. The mass absorption coefficient of Fe for Cu K_{α} radiation is large, 478 cm²/g. As a result of the absorption of Cu K_{α} from the source, iron then emits Fe K_{α} radiation that is independent of the detector angle and whether or not diffraction occurs. Consequently, the diffraction patterns of FeS₂ films tend to be noisy and have a baseline around 1000 cps due to the Fe K_{α} fluorescence.

Fluorescence was minimized in the diffraction pattern of FeS₂ by using a Cr filter to absorb Fe K_α radiation. The penetration of Cu K_α radiation into FeS₂ is described by Beer's Law

$$\frac{I_x}{I_0} = e^{-\mu x}$$

where I_x is the transmitted X-ray intensity, I_0 is the incident x-ray intensity, μ is the linear absorption coefficient (mass absorption coefficient divided by the density) and x is the distance through the medium. At 1° angle of incidence, Cu K_α radiation is estimated to penetrate the top 180 nm of a pyrite film, assuming that the surface is smooth.

We can take advantage of the variation of penetration depth of X-rays as a function of incident angle to probe the crystalline film at different depths. As mentioned above, grazing incidence where $\theta = 1^\circ$ only samples the upper most part of the film. At angles that satisfy the Bragg condition ($\theta > 1^\circ$) the X-ray beam penetrates deeply into the film giving diffraction data from the bulk of the material. A disadvantage of the $\theta - 2\theta$ geometry for thin films is that often the substrate is sampled as well as the overlaying film.

In order for constructive interference of X-rays to occur, they must be in phase with each other. After reflection from a crystal with a lattice spacing of d , two waves are in phase if the additional path length the second wave travels, l , is an integer

multiple of the wavelength, λ , of the first wave, Figure 2.9. The wavelength difference l between the two waves depends on the incoming wave's angle of incidence θ and the spacing d of the atomic planes. This leads to the condition

$$l = 2d\sin(\theta)$$

The overall pathway includes the distance of the incoming and outgoing waves, giving rise to the 2 in the equation. Therefore, the Bragg condition for constructive interference of scattered X-rays is given by

$$n\lambda = 2d\sin(\theta)$$

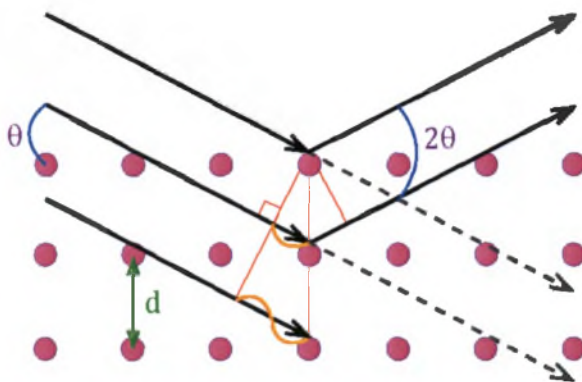
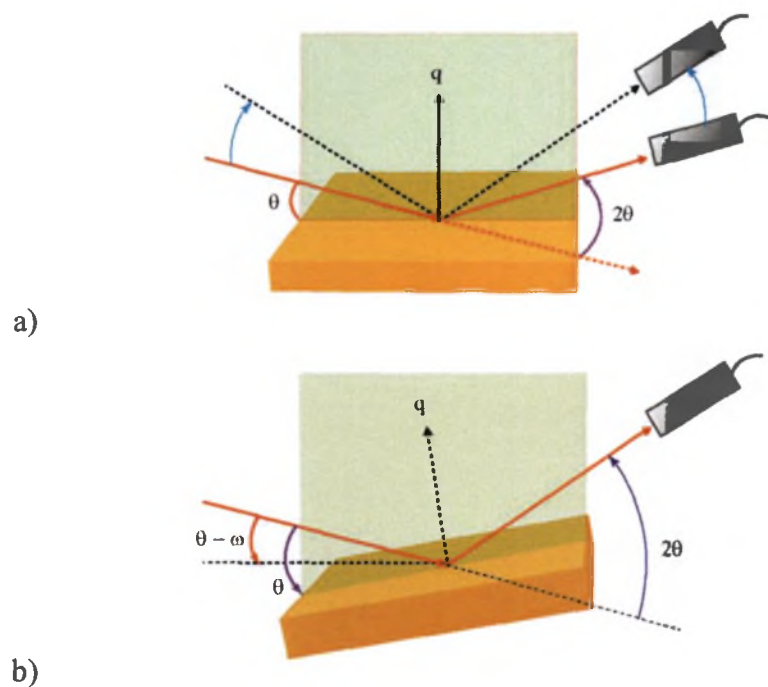


Figure 2.9. Ideal crystal lattice showing satisfaction of the Bragg condition λ shown in yellow.

For a typical powder diffraction pattern, the detector angle is twice the incident angle ($\theta - 2\theta$) in order to satisfy the Bragg condition. The sampling geometry can be one in which both the X-ray source and detector move synchronously by θ (Figure 2.10 a), or equivalently, the source can be stationary and the sample moves by θ while the detector scans over 2θ , as is the practice on the Bruker D8 at SFSU (Figure 2.10 b). In order to account for any mis-alignment of the substrate and thin film with respect to the incident X-ray beam, a small correction, ω , to the incident angle, θ , is often needed. The ω -correction is usually small, $< \pm 0.3$ degrees, and brings the substrate and thin film into perfect alignment with the X-ray beam. The so-called $2\theta - \omega$ scan is equivalent to the $\theta - 2\theta$ scan except for the direction of the scattering vector, \mathbf{q} . The scattering vector \mathbf{q} is normal to the substrate and thin film for the $2\theta - \omega$ geometry but not necessarily so for the $\theta - 2\theta$ geometry, and this affects the intensity of the Bragg peaks. The Bragg condition is strictly met for diffraction vectors (\mathbf{q}) that are normal to the surface of the film. As a result, the diffraction intensity is directly related to the orientation of grains within the polycrystalline film. If a pyrite thin film has preferred orientation, the intensity pattern will be different from a powder pattern and will exhibit peaks with greater or less intensity depending on the number of grains whose scattering vector \mathbf{q}_{hkl} is normal to the substrate.

In the grazing incidence geometry, Figure 2.10 c, the sample is held at a fixed angle with respect to the source and the detector is scanned through 2θ . All Bragg peaks may

be observed in the GIXRD geometry but the intensities do not indicate preferred orientation even if the intensity pattern is different from the powder pattern. The condition in which the scattering vector is normal to the thin film is called a symmetric scan (the specular reflectance condition) while the GIXRD geometry is an asymmetric scan. In this thesis, the three scattering geometries will be compared, but the GIXRD and $2\theta - \omega$ geometries will be emphasized because they sample the uppermost and bulk of the film, respectively.



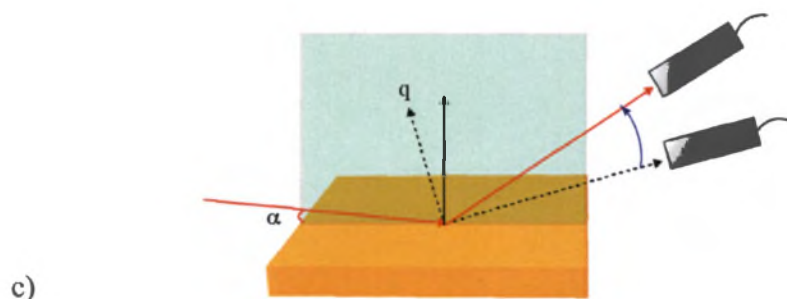


Figure 2.10. (a) Symmetric scan with moving source and moving detector, (b) symmetric scan with moving specimen and moving detector, (c) asymmetric scan.

Due to iron's strong K-edge at 7.11 keV, X-ray diffraction of pyrite thin films has high background counts, which can obscure weak peaks and contributes to noise in the diffraction pattern. To ensure that all pyrite peaks could be resolved, five diffraction patterns were acquired from each sample and the signal was averaged. In addition, the data were processed by the smoothing algorithm in the Bruker EVA analysis software. Smoothing the data lead to diffraction patterns with less noise so that even weak peaks were revealed. Care was taken during baseline and smoothing adjustments to ensure that false peaks were not generated. The result of the processing steps is compared in **Error! Reference source not found.** and leads to a diffraction pattern that reveals many peaks while minimizing noise. The smoothed, averaged, and baseline adjusted data (e.g., top trace in) are presented hereafter in the Results section of this thesis.

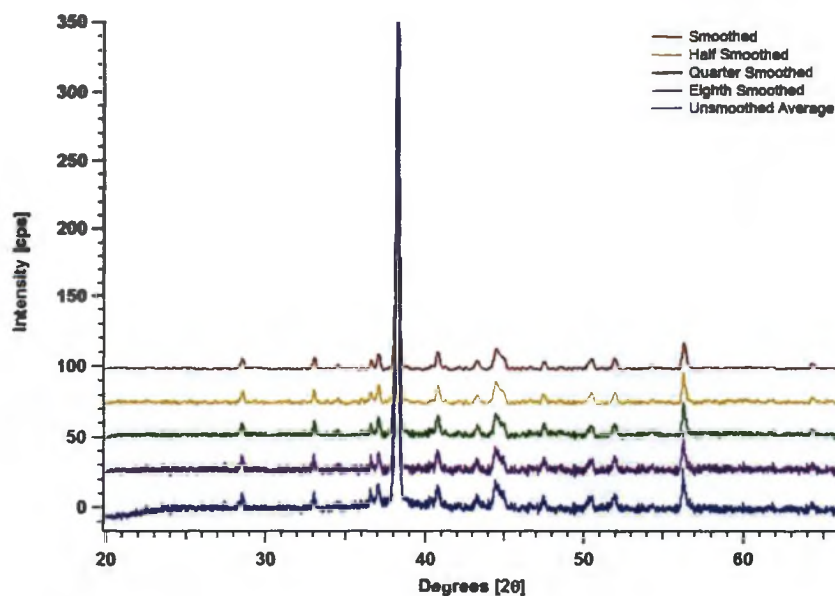


Figure 2.11. Average of five $2\theta - \omega$ XRD patterns as gathered and having been smoothed by half (0.075), a quarter (0.0375), an eighth (0.01875) as well as just smoothed (0.15).

2.2.3 Scanning Electron Microscopy

Scanning electron micrographs were acquired with a Carl Zeiss Ultra55 field emission scanning electron microscope (FESEM) equipped with an Everhart-Thornley (SE2) and through the lens (InLens) secondary electron detectors. The acceleration voltage and working distance typically used for imaging were between 2 keV and 5 keV with a working distance of 5 mm to 8.5 mm, respectively.

3 Results

There are two methods employed in this work to synthesize pyrite phase FeS_2 thin films. The first method (M1) involves the synthesis of Fe^{2+} molecular precursor

that is hydrothermally decomposed and the second (M2) employs ferric sulfate, sodium thiosulfate as a reducing agent, and sulfur.

3.1.1 Precursor Method (M1)

3.1.1.1 X-Ray Diffraction

Figure 3.1 compares X-ray diffraction patterns acquired from a thin film prepared using the precursor method with different X-ray scattering geometries. In this instance, the precursor was prepared two days in advance, collected, stored under vacuum, and then added to the Teflon liner with the Au/Si substrate and CTAB. The precursor concentration was 5 mM and the concentration of CTAB was 5.8 mM. The diffraction patterns were measured in $\theta - 2\theta$ (Figure 3.1a), $2\theta - \omega$ (Figure 3.1b), and $GI = 1^\circ$ (Figure 3.1c) geometries. A pyrite powder pattern from the literature (Figure 3.1d) is shown for comparison. The grazing incidence scattering geometry will be discussed first since it is straightforward to interpret.

The GIXRD pattern of the thin film (Figure 3.1c) shows that the major peaks correspond to those observed in the pyrite phase powder pattern, Figure 3.1d. The intensity pattern of the peaks is also similar to the literature intensities, except that the pyrite thin film (200) peak is less intense than the one in Figure 3.1d. Also observed in the GIXRD pattern is a small peak at 64.74° that is associated with the Au(220) reflection. Although the pyrite film shows good mechanical stability, the portion of the substrate that was inserted in the wafer holder has at most a very thin pyrite film or

simply bare gold substrate. Most films synthesized in this study had a small strip of bare gold at one edge of the film. As a result, both the thin FeS₂ film and the gold substrate were often sampled together in the GIXRD geometry. The GIXRD pattern confirms that the dominant phase at the surface of the film consists of almost pure pyrite and a trace of marcasite (211) reflection at ~52°.

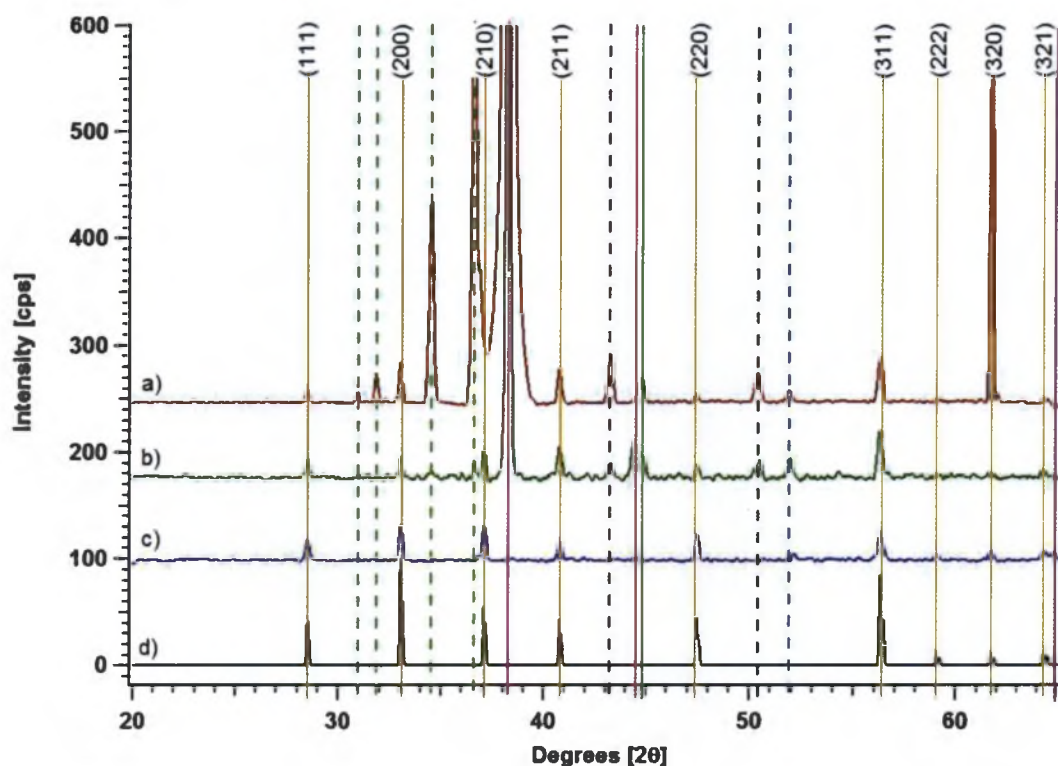


Figure 3.1. Method 1 film synthesized for 4.5 hours at 230 °C using the M1 with a) $\theta - 2\theta$ geometry, b) $\theta - \omega$ geometry, c) grazing incidence geometry and d) a pyrite powder pattern from literature. Yellow vertical lines indicate the expected peaks from the pyrite phase of FeS₂ with the Miller indices noted at the top. Green dashed lines indicate W L α contamination, pink lines indicate the Au peaks, black dashed lines indicate the copper holder, the green line is likely an FeS species, and the dark blue dashed line is the marcasite (211) reflection at ~52°.

Additional peaks in the $\theta - 2\theta$ pattern are ascribed to artifacts. For example, the tungsten (W) $L_{\alpha 1}$ line also samples the gold substrate and results in the observation of the Au(111) reflection at 36.52° . The cathode in the X-ray source is a W filament that operates at 40 kV and 40 mA. Over time, W is deposited on the Cu anode. The W deposited on the anode then serves as a secondary source of X-rays; in particular, W $L_{\alpha 1}$, $L_{\alpha 2}$, $L_{\beta 1}$, and $L_{\beta 2}$ lines have wavelengths of 1.4764 Å, 1.4875 Å, 1.2818 Å, and 1.2446 Å, respectively. The copper K_{β} line (1.3922 Å) also served as source and the Au(111) peak appears at 34.5° (note that after adjustment of the Goebel mirror, the K_{β} line was no longer observed). Two other spurious lines in the $\theta - 2\theta$ pattern are observed at $31.0^\circ 2\theta$ and $31.9^\circ 2\theta$ and are also ascribed to source impurities.

Table 1 shows the location and relative area of each pyrite peak for the XRD patterns shown in Figure 3.1. The main conclusion from Table 1 is that the precursor method results in a thin pyrite film since the film peaks have a one-to-one correspondence to the powder pattern from the literature. In addition, the location of each peak is within 0.05° of the literature pattern regardless of the XRD scattering geometry. Thus, all three scattering geometries could be used to determine if pyrite is present. The area of each peak is scaled to the most intense peak of the powder pattern corresponding to the (311) peak at 56.35° . However, the intensities of the other reflections do not match the powder pattern and will be discussed further below. The W $L_{\alpha 1}$ X-ray line produces a Au(111) peak that obscures the pyrite (210) at 37.12° . In

addition, there is an anomalous peak at 61.74° . Although the peak at $61.74^\circ 2\theta$ corresponds to the pyrite (320), it is narrower than what is expected for a pyrite peak at that angle and far too intense, with a relative area $> 900\%$. In all geometries of the film grown with CTAB at 230°C , the (311) has the greatest relative area.

Table 1. Peak locations and areas (relative to the (311) peak) for the pyrite phase Miller indices between $2\theta = 0$ and $2\theta = 66$ for $\theta - 2\theta$, $2\theta - \omega$ and GI XRD geometries of a film synthesized for 4.5 hours at 230°C using the precursor method with CTAB. Dashes indicate no peak present.

Miller Index (hkl)	From Literature ³⁶		$\theta - 2\theta$		$2\theta - \omega$		Grazing Incidence	
	$^\circ 2\theta$	Rel Area	$^\circ 2\theta$	Rel Area	$^\circ 2\theta$	Rel Area	$^\circ 2\theta$	Rel Area
(111)	28.55	39.20	28.54	0.03	28.52	31.50	28.53	54.02
(200)	33.08	95.54	33.03	60.93	33.04	30.15	33.07	91.71
(210)	37.12	54.87	--	--	37.08	43.70	37.11	99.38
(211)	40.81	45.48	40.77	50.76	40.78	59.55	40.80	56.41
(220)	47.48	51.01	47.43	0.29	47.47	23.24	47.47	77.00
(311)	56.30	100.00	56.29	100.00	56.29	100.00	56.33	100.00
(222)	59.08	15.84	--	--	--	--	59.04	16.98
(320)	61.75	16.11	*	*	--	--	61.74	30.08
(321)	64.32	15.90	--	--	64.28	17.77	64.53	79.84

*Anomalous peak in $\theta - 2\theta$ XRD pattern.

It is reiterated that the Bragg condition is strictly met in the $\theta - 2\theta$ geometry for families of planes that are parallel to the surface, the so-called specular reflection condition. Mounting a thin film on the home-built thin film holder always requires a correction factor omega (ω) to ensure that diffraction is measured under specular conditions. Typically, the correction factor to the incident angle, ω , is small $\leq \pm 0.3^\circ$, but this difference has a surprising effect on peak intensities, cf., Figure 3.1 a and b. The $2\theta - \omega$ geometry employs a small correction (ω) to the incident angle and brings

the thin pyrite film into specular reflection condition. Under specular conditions, the measured peak intensities for a given set of lattice planes (hkl) of a thin film can be compared to the powder pattern. Any difference between the powder pattern and thin film intensities may indicate preferred orientation in the thin film. Therefore, XRD data of thin films will compare the $2\theta - \omega$ and GIXRD patterns in the remainder of this thesis.

Table 2 and Table 3 compare the peak location and relative areas of XRD peaks observed for films measured under specular $2\theta - \omega$ and GIXRD conditions and compare these to the literature powder pattern. The films were prepared by the precursor M1 method without surfactant at 230 °C for three time periods, 1.5 hr, 3 hr, and 4.5 hr. The first observation is that pyrite is the primary result of the synthesis from 1.5 – 4.5 hr. For films grown without surfactant, peak positions match the literature values well for both $2\theta - \omega$ and GIXRD conditions. To facilitate a comparison of intensities under specular conditions (Table 2), pink fields indicate peaks with higher relative areas than the literature and blue fields indicate smaller relative areas than the literature powder pattern. It is observed that the pyrite (111) and (211) reflections have greater intensity than the literature pattern, while peaks with Miller indices (200), (210), and (220) are less intense. The weakest peaks of the pyrite powder pattern have indices (222) and (320) and are weak or not observed in the $2\theta - \omega$ geometry. However, they are observed in the GIXRD geometry. The (311) peak remains the most intense. The (321) peak does not appear in the 1.5 hour

synthesis, but in the 3 hour and 4.5 hour synthesis it increases in relative area. The 1.5 hour synthesis has the fewest pyrite phase FeS₂ peaks, with the (220), (222), (320) and (321) reflections missing.

Table 2. Location and relative areas by $2\theta - \omega$ XRD of films grown without surfactant at 230 °C using the precursor method for 1.5, 3 and 4.5 hours. All peak areas have been scaled to the (311) pyrite peak. All locations are reported in degrees 2θ . Dashes indicate no peak present.

(hkl)	Literature		1.5 Hours		3 Hours		4.5 Hours	
	$^{\circ}2\theta$	Rel Area						
(111)	28.55	39.20	28.52	66.01	28.52	43.50	28.49	50.10
(200)	33.08	95.54	33.05	34.12	33.05	20.47	33.01	55.51
(210)	37.12	54.87	37.07	49.31	37.07	27.66	37.04	60.32
(211)	40.81	45.48	40.74	78.80	40.78	72.68	40.74	74.60
(220)	47.48	51.01	--	--	47.46	14.99	47.44	32.05
(311)	56.30	100.00	56.26	100.00	56.31	100.00	56.28	100.00
(222)	59.08	15.84	--	--	59.03	15.98	--	--
(320)	61.75	16.11	--	--	--	--	--	--
(321)	64.32	15.90	--	--	64.33	24.72	64.30	33.77

Table 3. Location and relative areas by GI XRD of films grown without surfactant at 230 °C using the precursor method for 1.5, 3 and 4.5 hours. All peak areas have been scaled to the (311) pyrite peak. All locations are reported in degrees 2θ . Dashes indicate no peak present.

(hkl)	Literature		1.5 Hours		3 Hours		4.5 Hours	
	$^{\circ}2\theta$	Rel Area						
(111)	28.55	39.20	28.52	99.21	28.53	175.74	28.52	108.07
(200)	33.08	95.54	33.05	64.76	33.08	80.93	33.05	93.59
(210)	37.12	54.87	37.10	122.07	37.11	219.96	37.10	118.87
(211)	40.81	45.48	40.80	63.57	40.81	81.22	40.80	68.83
(220)	47.48	51.01	47.46	92.95	47.47	153.19	47.46	86.51
(311)	56.30	100.00	56.31	100.00	56.33	100.00	56.32	100.00
(222)	59.08	15.84	--	--	--	--	59.11	10.09
(320)	61.75	16.11	61.73	34.68	61.74	60.27	61.72	32.82
(321)	64.32	15.90	64.75	356.38	64.29	30.62	64.34	43.57

Table 4. Location and relative areas by $2\theta - \omega$ XRD of films grown with surfactant at 230 °C using the precursor method for 1.5, 3 and 4.5 hours. All peak areas have been scaled to the (311) pyrite peak. All locations are reported in degrees 2θ . Dashes indicate no peak present.

(hkl)	Literature		1.5 Hours		3 Hours		4.5 Hours	
	$^{\circ}2\theta$	Rel Area						
(111)	28.55	39.20	28.50	18.34	28.52	13.46	28.52	31.50
(200)	33.08	95.54	33.01	52.31	33.03	100.28	33.04	30.15
(210)	37.12	54.87	37.06	42.16	37.08	49.34	37.08	43.70
(211)	40.81	45.48	40.75	53.77	40.76	43.47	40.78	59.55
(220)	47.48	51.01	47.42	28.80	47.42	25.63	47.47	23.24
(311)	56.30	100.00	56.27	100.00	56.26	100.00	56.29	100.00
(222)	59.08	15.84	--	--	--	--	--	--
(320)	61.75	16.11	61.63	21.02	--	--	--	--
(321)	64.32	15.90	--	--	--	--	64.28	17.77

Table 5. Location and relative areas by GI XRD of films grown with surfactant at 230 °C using the precursor method for 1.5, 3 and 4.5 hours. All peak areas have been scaled to the (311) pyrite peak. All locations are reported in degrees 2θ . Dashes indicate no peak present.

(hkl)	Literature		1.5 Hours		3 Hours		4.5 Hours	
	$^{\circ}2\theta$	Rel Area						
(111)	28.55	39.20	28.49	50.10	28.53	15.38	28.53	54.02
(200)	33.08	95.54	33.01	55.51	33.06	156.80	33.07	91.71
(210)	37.12	54.87	37.04	60.32	37.08	85.63	37.11	99.38
(211)	40.81	45.48	40.74	74.60	40.80	44.99	40.80	56.41
(220)	47.48	51.01	47.44	32.05	47.46	50.22	47.47	77.00
(311)	56.30	100.00	56.28	100.00	56.31	100.00	56.33	100.00
(222)	59.08	15.84	--	--	59.04	15.73	59.04	16.98
(320)	61.75	16.11	--	--	61.77	27.33	61.74	30.08
(321)	64.32	15.90	64.30	33.77	64.38	37.97	64.53	79.84

Peak positions match well for films grown with surfactant as well. There is an increase in the relative areas for the (210) reflection, but not for the (111) and (200). The (111), (210) and the (220) peaks show a decrease in relative area compared to the (311) peak. Similar to the films grown without surfactant, the ones grown with surfactant show fewer peaks above $56^{\circ} 2\theta$, with only the (320) reflection appearing in the 1.5 hour synthesis and the (321) reflection appearing in the 4.5 hours synthesis.

Figure 3.2 shows three graphs of the three XRD geometries with intensity on the y-axis and the angle, 2θ , on the x-axis. The green traces are films with surfactant and the red traces are films synthesized without. Dashed lines represent the pyrite (200) and the marcasite (101) Miller indices. The $\theta - 2\theta$ geometry clearly shows that films held at temperature (230 °C) for longer periods produce more of the pyrite phase. If marcasite were present, a shoulder would appear at 33.2° or the overall peak envelope would be broader.

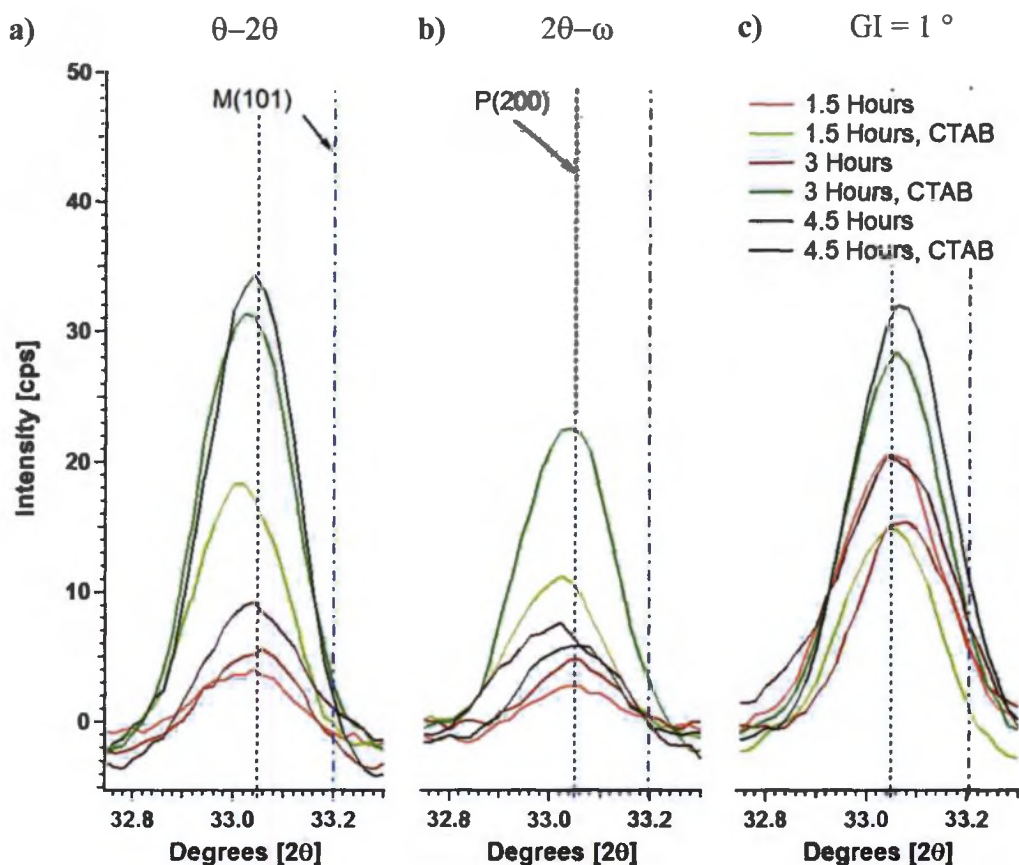


Figure 3.2. X-ray diffraction patterns showing the range between 32.75 2θ and 33.25 2θ by a) locked coupled geometry, b) unlocked coupled geometry, and c) grazing incidence geometry for three different synthesis times with and without CTAB.

Additionally, we see an increase of the intensity of this peak with the addition of surfactant. The $2\theta - \omega$ geometry does not give the same orientation information that the $\theta - 2\theta$ geometry does, but still shows that increased times promote the growth of the pyrite phase. The $2\theta - \omega$ and GI geometry also show the increase of the pyrite phase at the surface and the assist given by the surfactant. In the $\theta - 2\theta$ geometry, the syntheses with surfactant show the peak shifting slightly to the right. The syntheses without surfactant have a shoulder, particularly notable in the 4.5 hour synthesis, that corresponds to the marcasite (101) peak.

Cubic pyrite phase FeS_2 has the lattice constant $a = b = c = 5.417 \text{ \AA}$.³⁷ The lattice constant was calculated from the (200) reflection using the equation:

$$a = d_{hkl} \sqrt{h^2 + k^2 + l^2}$$

which is derived from the Bragg equation. The d-spacing was found by fitting each diffraction pattern with the fitting program EVA. The excellent agreement between experimental and literature values suggests that the pyrite phase has good crystallinity without many bulk defects.

Table 6. Lattice constant of M1 films with and without surfactant calculated from the (200) d-spacing. D-spacing found from the (311) reflection noted with an asterisk. Actual lattice constant of pyrite has been determined to be 5.418 Å.³⁷

Method 1	Grazing Incidence	Unlocked Coupled
1.5 Hours, no CTAB	5.412 Å	5.415 Å
3 Hours, no CTAB	5.413 Å	5.415 Å
4.5 Hours, no CTAB	5.414 Å	5.420 Å*
Average	5.413 Å	5.417 Å
1.5 Hours, CTAB	5.417 Å	5.416 Å
3 Hours, CTAB	5.415 Å	5.415 Å
4.5 Hours, CTAB	5.413 Å	5.421 Å
Average	5.415 Å	5.417 Å

3.1.1.2 Scanning Electron Microscopy

Scanning electron microscopy images of films synthesized without CTAB

(Figure 3.3) consist of blocky crystals. It is evident from Figure 3.3 that these films are rough and are not continuous. Large areas of exposed Au substrate indicate that nucleation on the surface is probably sparse. Crystal size varies from the 10's of nanometers to crystals as large as 2 µm. Cross section images of the films shown in Figure 3.4 show that the crystal grains extend from the substrate to the external surface

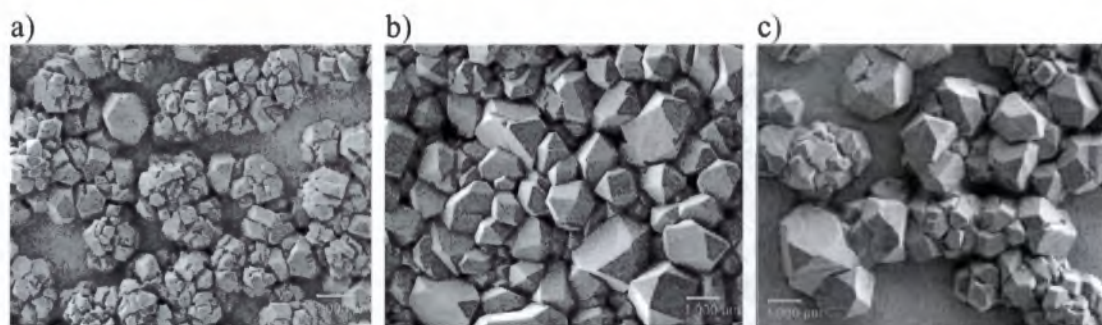


Figure 3.3. Secondary electron micrographs acquired of M1 films synthesized without CTAB for a) 1.5 hours, b) 3 hours, and c) 4.5 hours. All films had 6 mM of precursor and were synthesized at 230° C.

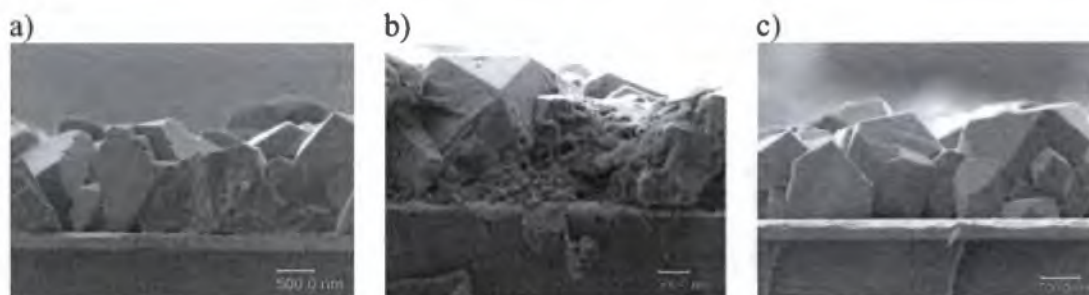


Figure 3.4. Edge view secondary electron micrographs acquired of M1 films synthesized without CTAB for a) 1.5 hours, b) 3 hours, and c) 4.5 hours. All films had 6 mM of precursor and were synthesized at 230° C.

of the film and are often similar in size at the substrate as at the surface of the film (Figure 3.4). Thickness of the films are on the order of the larger crystals, up to 2 μm .

Films synthesized by M1 with surfactant are continuous showing no evidence for bare substrate and the crystallites have a size range between 0.05 -1.5 μm (Figure 3.5). In general, the crystals are smaller and granular at the substrate and large and blocky at the surface (Figure 3.6). We can infer that

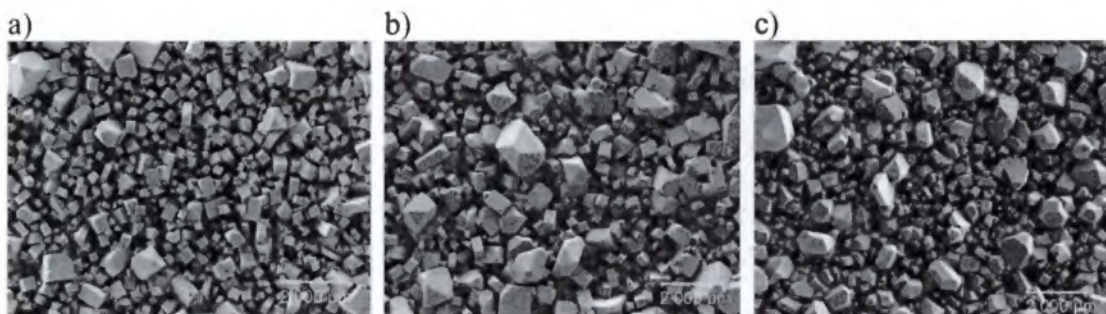


Figure 3.5. Secondary electron micrographs acquired of M1 films synthesized with CTAB for a) 1.5 hours, b) 3 hours, and c) 4.5 hours. Films had 5 mM, 5.8 mM and 5.8 mM of precursor respectively, and were synthesized at 230° C.

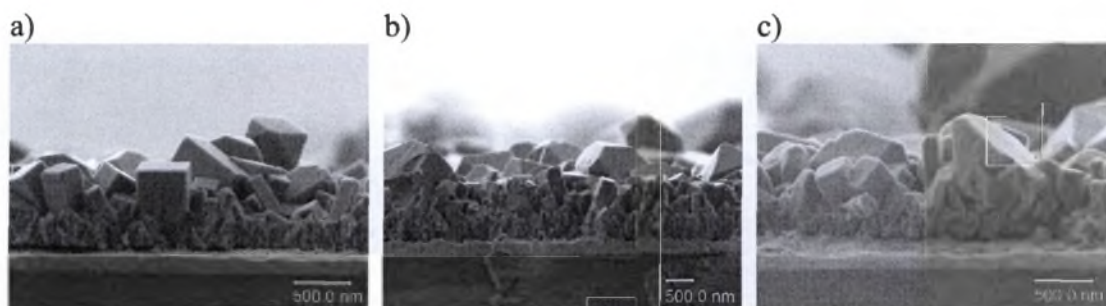


Figure 3.6. Edge view secondary electron micrographs acquired of M1 films synthesized with CTAB for a) 1.5 hours, b) 3 hours, and c) 4.5 hours. Films had 5 mM, 5.8 mM and 5.8 mM of precursor respectively, and were synthesized at 230° C.

nucleation is denser in the presence of CTAB leading to many small crystallites at the substrate interface that later differentiate into blocky crystals as the film grows. While it may seem from these micrographs that certain films have a larger ratio of larger-to-smaller crystals than others, as in Figure 3.5, that is not really the case. The entire surface of the films have regions of larger crystals and regions of more surface defects as can be seen in Figure 3.7. This observation generally holds true for films prepared by both M1 and M2 methods.

Concentration of surfactant effected the crystal size and surface roughness of the films. Higher concentrations of surfactant resulted in films with rougher surfaces with blocky crystals and thinner films, while lower concentrations of surfactant resulted in smoother films with small granular crystals and thicker overall films, as seen in Figure 3.8 to Figure 3.11.

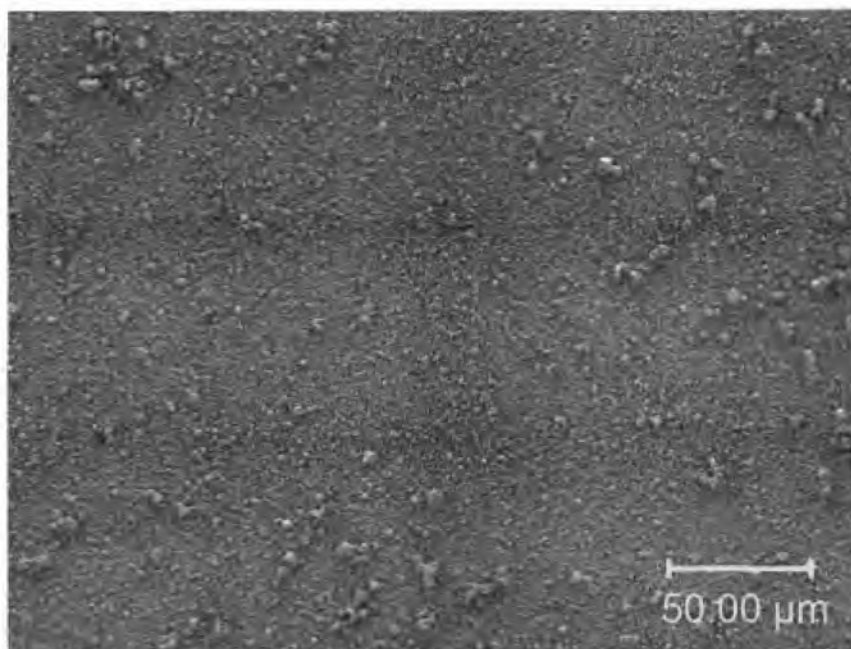


Figure 3.7. Secondary electron micrograph acquired of M1 film synthesized with CTAB for 3 hours. Film had 5.8 mM of precursor, and was synthesized at 230° C.

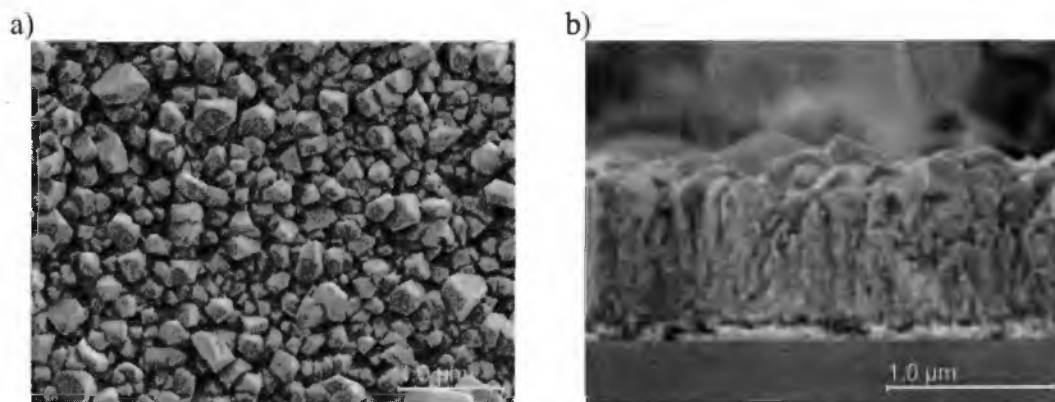


Figure 3.8. Film synthesized with 20 mM FeCl_3 , 35 mM DDAS and 40 mM CTAB at 230 °C for four hours.

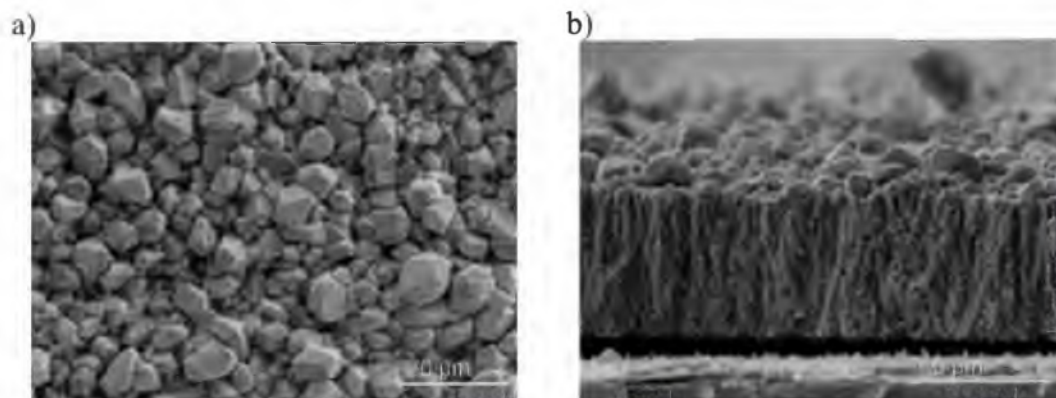


Figure 3.9. Film synthesized with 20 mM FeCl_3 , 35 mM DDAS and 20 mM CTAB at 230 °C for four hours.

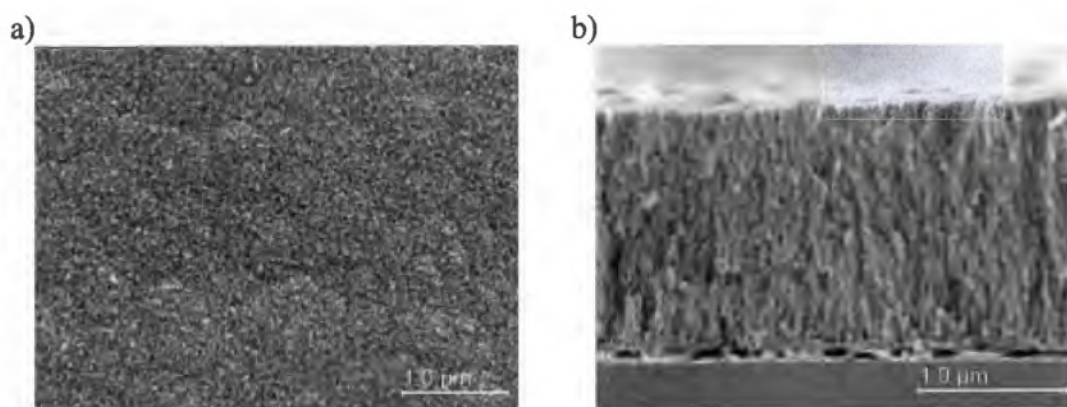


Figure 3.10. Film synthesized with 20 mM FeCl_3 , 35 mM DDAS and 15 mM CTAB at 230 °C for four hours.

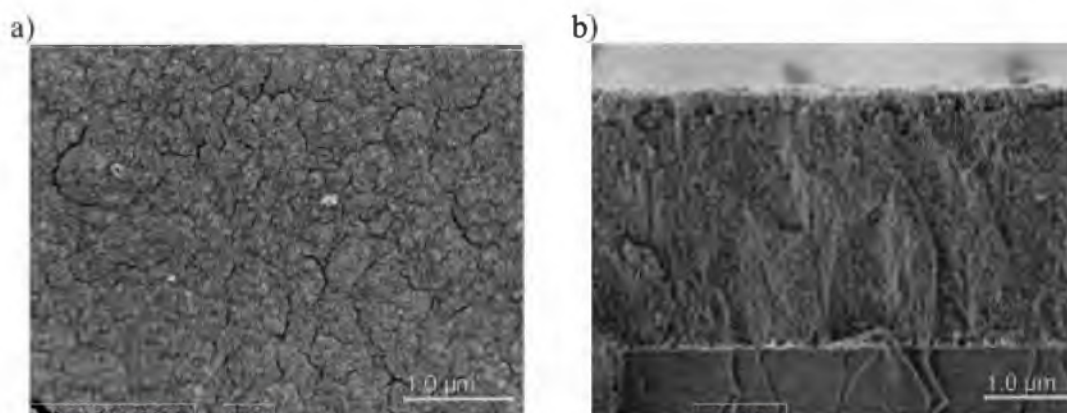


Figure 3.11. Film synthesized with 20 mM FeCl_3 , 35 mM DDAS and 10 mM CTAB at 230 °C for four hours.

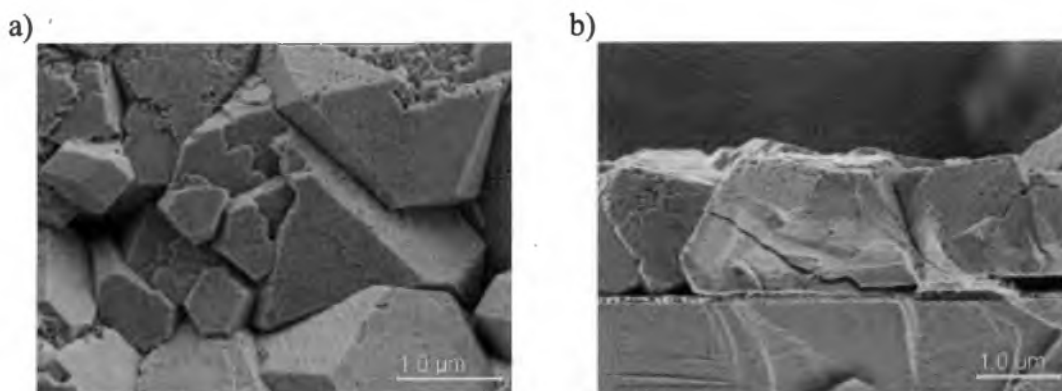


Figure 3.12. Film synthesized with 20 mM FeCl₃, 35 mM DDAS and 0 mM CTAB at 230 °C for four hours.

. The smoothness of the films seen in Figure 3.10 and Figure 3.11 was sufficient to make the films visibly shiny and reflective. The thickness of the films decreased with higher concentrations of surfactant (Table 7.). GIXRD of these films shows that the pyrite phase is present in all films. All the major marcasite peaks appear in the film synthesized without CTAB and the marcasite (211) peak is observed in the film synthesized with 10 mM CTAB. The intensity of all the pyrite peaks increases with increasing concentrations of CTAB.

Table 7. Thickness of films synthesized with surfactant for 4 hours with 20 mM FeCl₃ and 35 mM DDAS.

CTAB	Thickness
40 mM	768 nm
20 mM	1 μm
15 mM	1.6 μm
10 mM	2.9 μm
0 mM	1.6 μm

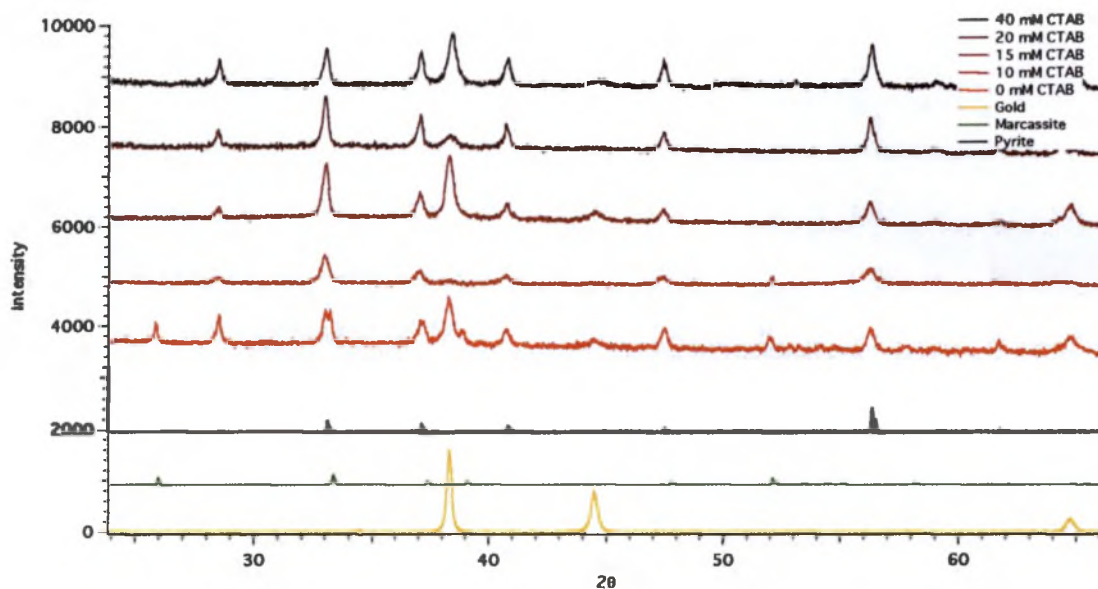


Figure 3.13. GIXRD of films synthesized with 20 mM FeCl_3 , 35 mM DDAS and 40, 20, 15, 10, and 0 mM CTAB, respectively, at 230 °C for four hours.

Given the smoothness of the films synthesized with 10 mM CTAB and 15 mM CTAB, two sets of films were synthesized with 4 mM, 5 mM, 9 mM, and 13 mM to determine if the surface roughness and crystal size and shape could be repeated in the films. While lower concentrations of surfactant do produce films with smaller crystal sizes at the surface of the films, there is still an enormous variation in the morphology of the films. The surfaces of these films, shown in Figure 3.14 through Figure 3.17, also vary across the surface of the individual film and all contain surface defects, which are cracks in the film or artifacts, an obvious example is seen in Figure 3.17 b. GIXRD of these films gave weak signal to noise traces, but the films contain the pyrite phase and very little or no marcassite. A typical GIXRD scan is seen in Figure 3.19.

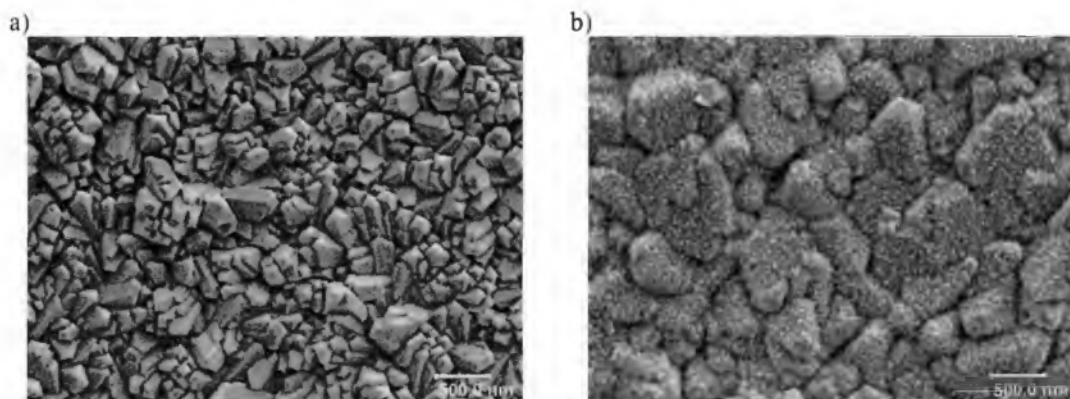


Figure 3.14. Two films synthesized with 10 mM FeCl_3 , 19 mM DDAS and 4 mM CTAB for a 4 hour hold at 230 °C.

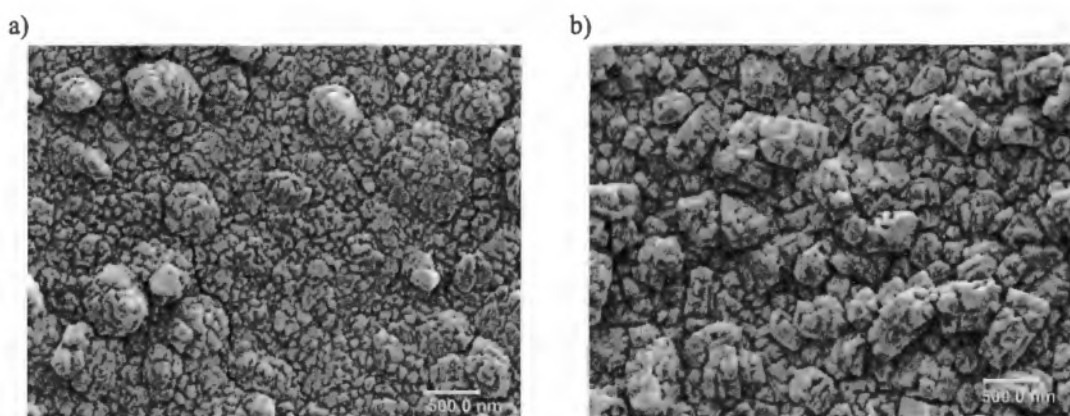


Figure 3.15. Two films synthesized with 10 mM FeCl_3 , 19 mM DDAS and 5 mM CTAB for a 4 hour hold at 230 °C.

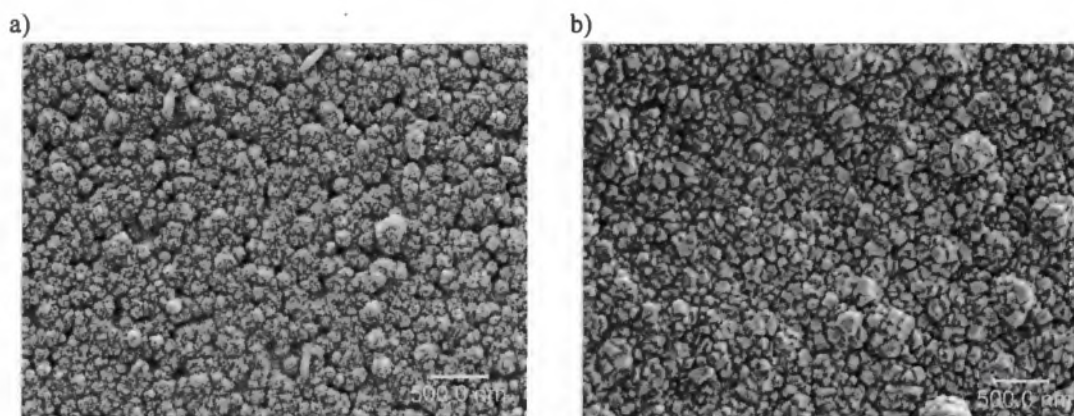


Figure 3.16. Two films synthesized with 10 mM FeCl₃, 19 mM DDAS and 9 mM CTAB for a 4 hour hold at 230 °C.

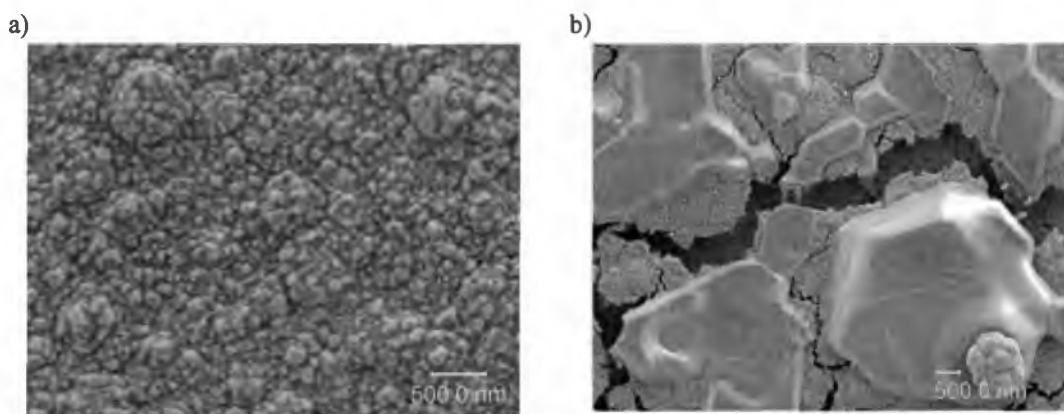


Figure 3.17. Two films synthesized with 10 mM FeCl₃, 19 mM DDAS and 13 mM CTAB for a 4 hour hold at 230 °C.

The large peak at $64.82^\circ 2\theta$ can be attributed to the Au(220) peak of the substrate.

Edge view micrographs of some these films, seen in Figure 3.18, show that the films have small granular crystals throughout the films, Figure 3.18 b.

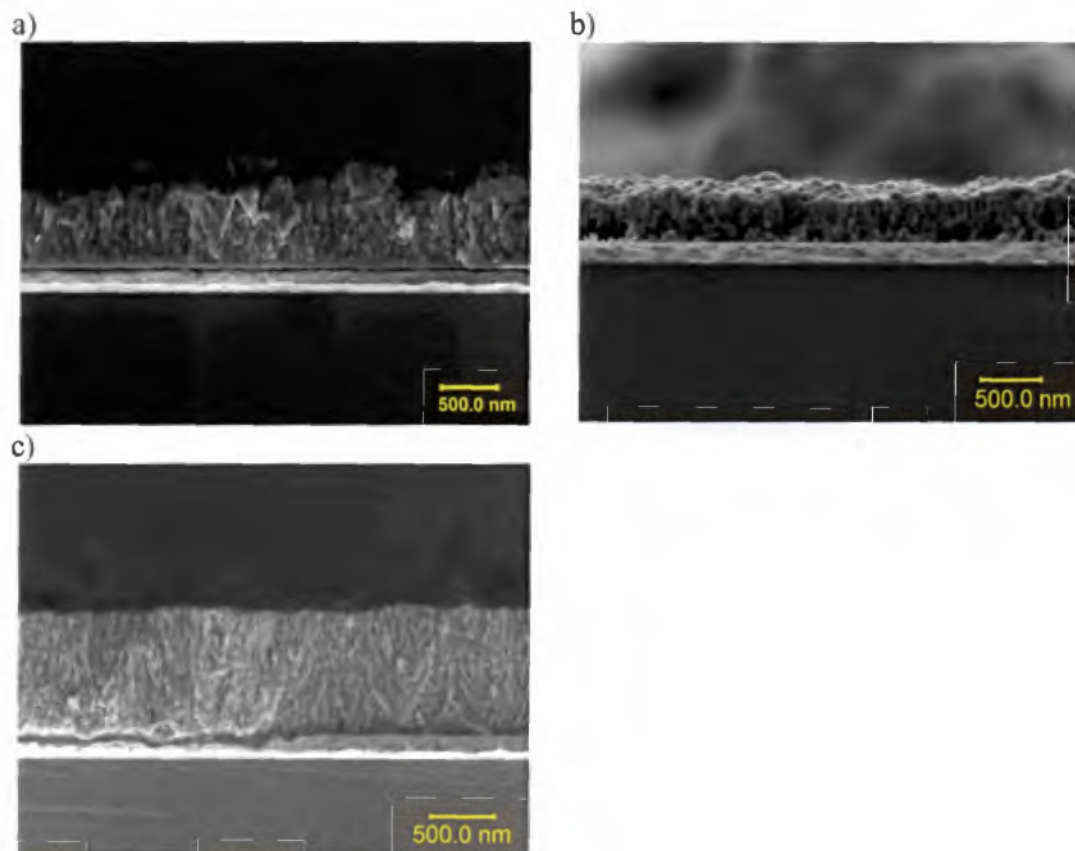


Figure 3.18. Films synthesized with 10 mM FeCl_3 and 19 mM DDAS with a 4 hour hold at 230 °C with CTAB concentrations of a) 5 mM, b) 9 mM and c) 13 mM.

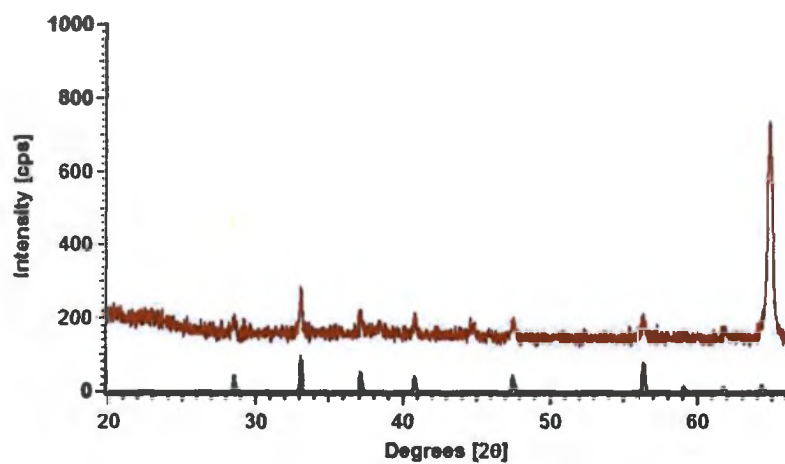


Figure 3.19. GIXRD of film synthesized with 10 mM FeCl_3 , 19 mM DDAS and 5 mM CTAB for a 4 hour hold at 230 °C.

3.1.2 Sulfate Salt Method (M2)

Films made by the sulfate salt method showed the presence of marcasite in significant amounts in every instance, although the addition of base increases the amount of the pyrite phase. The films without pH adjustment have plate-like crystals that increase in thickness as the temperature increases (Figure 3.20 a-c). The crystals extend from the substrate to the surface of the film and have thicknesses of 5 to 7 μm (Figure 3.21).

Hollow tube structures were observed in the film

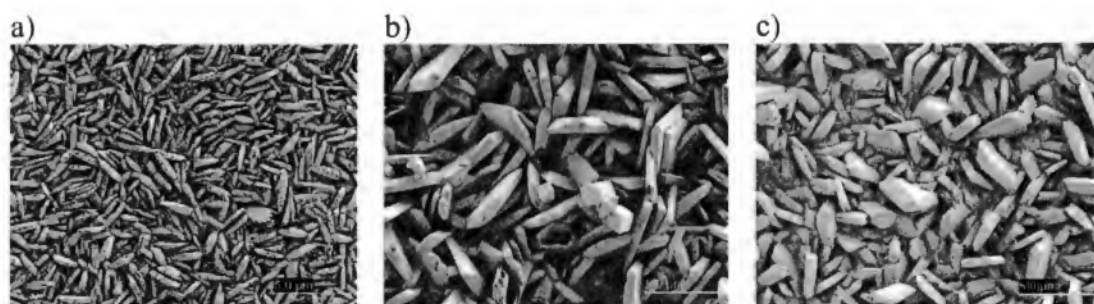


Figure 3.20. M2 films synthesized without pH adjustment at a) 150 °C, b) 190 °C, 230 °C.

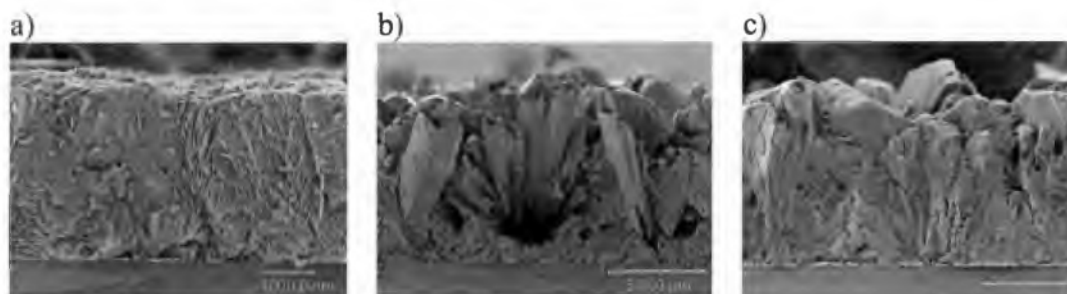


Figure 3.21. Cross sections of M2 films synthesized without pH adjustment at a) 150 °C, b) 190 °C, 230 °C.

synthesized at 190 °C. GIXRD of these films shows the (101) and (211) marcasite peaks are observed in all, with no pyrite peaks observed (Figure 3.22). There are unidentified peaks, marked with asterisks, that do not correspond to the pyrite phase or the marcasite phase.

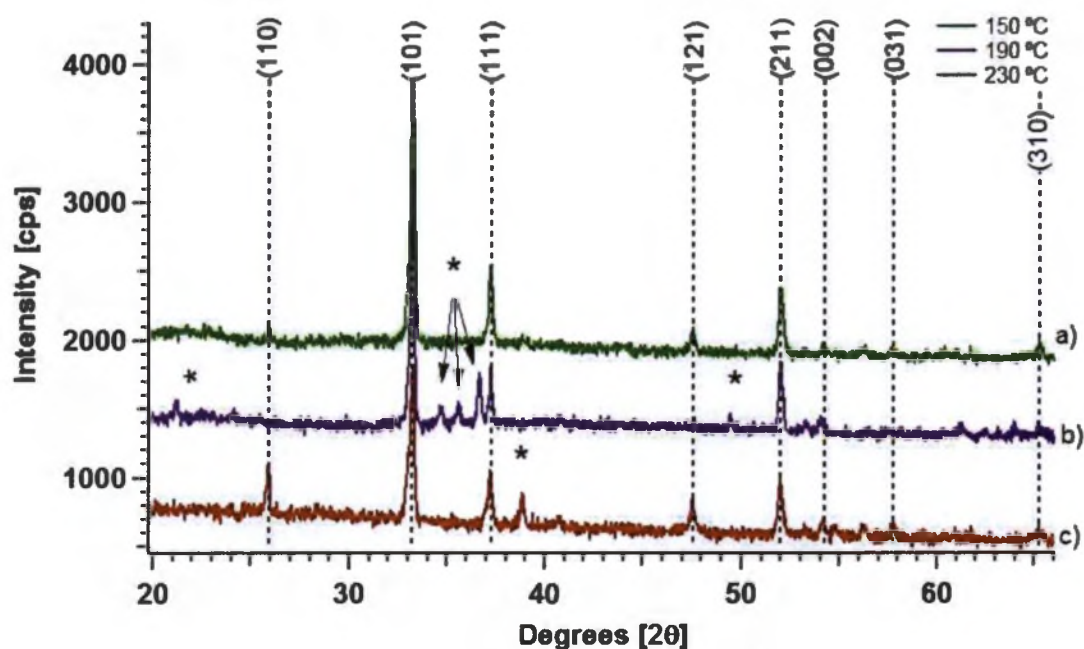


Figure 3.22. GIXRD of films synthesized with 20 mM FeSO_4 and 20 mM $\text{Na}_2\text{S}_2\text{O}_3$ at a) 150 °C, b) 190 °C and c) 230 °C with a beginning pH of ~2.

For films synthesized at 250 °C with the pH adjusted to ~6, the thickness of the plate-like crystals become thicker and there are fewer defects variations of crystal habits (Figure 3.23). The films are continuous, extend from the substrate to the surface of the film and have rough surfaces (Figure 3.24).

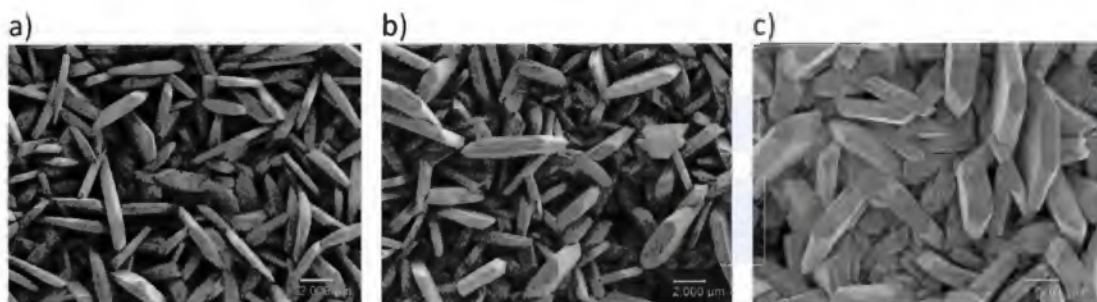


Figure 3.23. M2 films synthesized with 33 mM FeSO_4 and 33 mM $\text{Na}_2\text{S}_2\text{O}_3$ at 250 °C with a) 9 mM NaOH and pH 4.5, b) 14 mM NaOH and pH 6, c) 17 mM NaOH and pH 7.

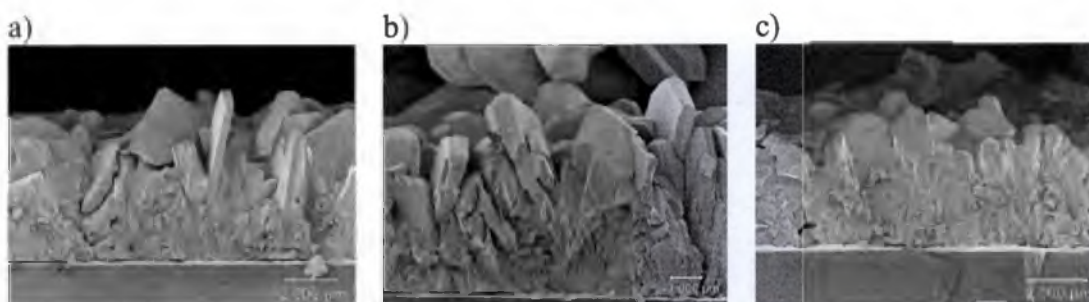


Figure 3.24. Cross sections of M2 films synthesized with 33 mM FeSO_4 and 33 mM $\text{Na}_2\text{S}_2\text{O}_3$ at 250 °C with a) 9 mM NaOH and pH 4.5, b) 14 mM NaOH and pH 6, c) 17 mM NaOH and pH 7.

GIXRD of these films indicate that there is some of the pyrite phase present, marked with yellow lines in Figure 3.25. There is not a significant increase in the pyrite phase as the pH is increased. When sufficient NaOH is added to the reaction, the pH does not increase above 7 and a green precipitate forms in solution. Figure 3.26 of just the area around the dominant pyrite (200) peak at $33.05\ 2\theta$ and the marcasite (101) peak at $33.20\ 2\theta$ show that there is possibly some pyrite (200), but

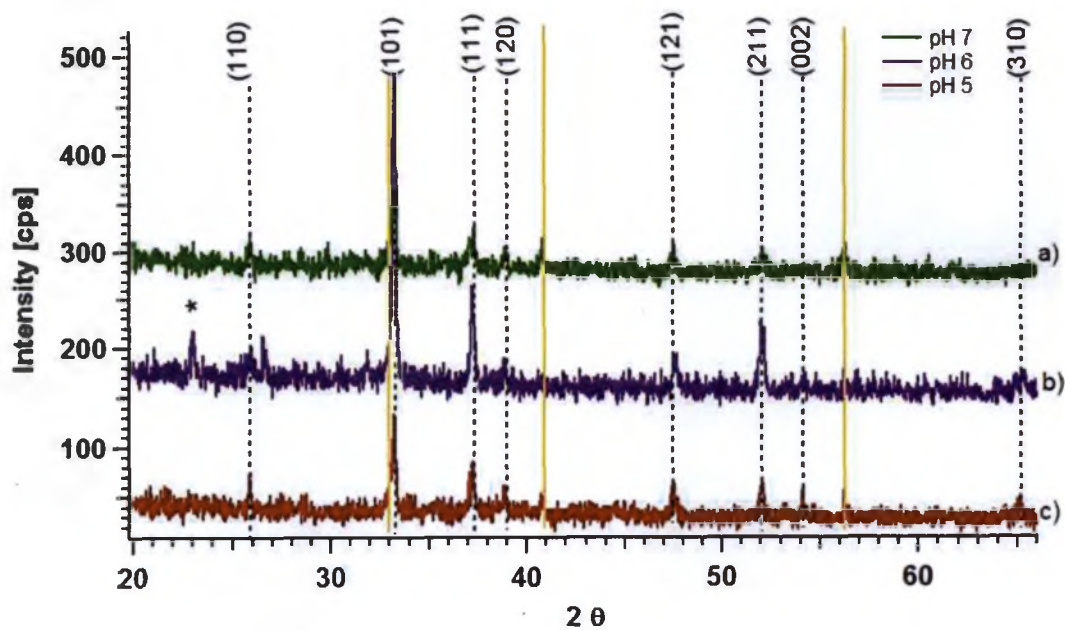


Figure 3.25. GIXRD of films synthesized at 250 °C with 33 mM FeSO_4 , 33 $\text{Na}_2\text{S}_2\text{O}_3$, with a) pH 7, b) pH 6, c) pH 5.

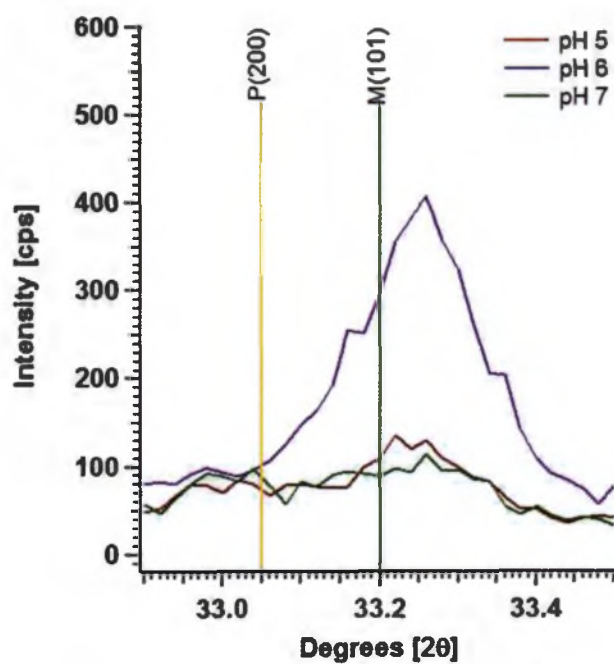


Figure 3.26. GIXRD of films synthesized at 250 °C with 33 mM FeSO_4 , 33 $\text{Na}_2\text{S}_2\text{O}_3$.

the signal to noise is too low to be sure. However, the dominant marcasite phase, variation in the crystal habit, and high rate of defects in the films and powders make this method unsuitable for an effective electron transport layer, and the method was not pursued. Figure 3.27 a shows a M1 powder and three films (Figure 3.27 b-c) that illustrate some of the crystal habits that were observed.

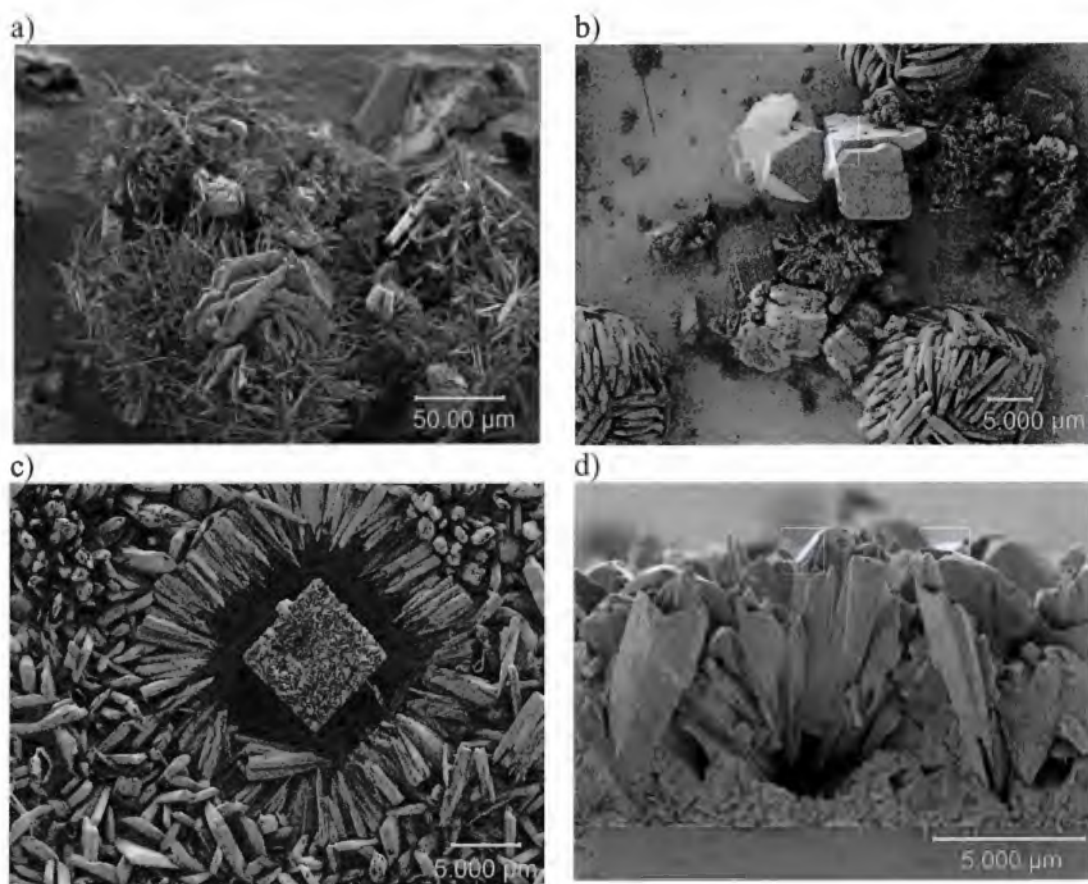


Figure 3.27. a) M1 powder made with 150 mM FeSO_4 , 150 mM $\text{Na}_2\text{S}_2\text{O}_3$, at 230 °C for 20 hours, b) M1 film made with 4 mM FeSO_4 , 3 mM $\text{Na}_2\text{S}_2\text{O}_3$, at 230 °C for 20 hours, c) M1 film made with 34 mM FeSO_4 , 34 mM $\text{Na}_2\text{S}_2\text{O}_3$ at 190 °C, d) edge view of preparation shown in c).

4 Summary and Conclusion

Two synthetic approaches that Wadia et al.³⁴ and Wu et al.³³ (M1 and M2, respectively) employed to successfully synthesize the pyrite phase of FeS₂ were adapted to synthesize the pyrite phase as a thin film.

For M1 films, the GIXRD and $2\theta - \omega$ scans give pyrite with the same peak positions and lattice constant as literature values, while M2 gave marcasite with some traces of pyrite in films with a starting pH of ~ 6 (Figure 3.25). The $2\theta - \omega$ scans for method M1 do not have intensity patterns identical to powder patterns but show some variation with the (211) reflection being consistently larger. This may indicate weak preferred orientation with (211) and (311) lattice planes parallel to the substrate. The trend for peak intensities based on M1 with and without CTAB is that peaks with Miller indices ($hk1$) are slightly more intense while those with Miller indices with zero in the l -index ($hk0$) are somewhat weaker. The intensity variation with l -index may indicate weak preferred orientation.

Trace amounts of marcasite are observed in thin films prepared by M1 at 51.9 °2 θ , (211) reflection, in some $2\theta - \omega$ scans but not in GIXRD, with or without the presence of surfactant. This suggests that marcasite is an impurity phase that sometimes appears early in the synthesis, perhaps during initial growth at lower temperatures before the temperature of the Parr reactor reached 230 °C. However, that the marcasite (101) peak, which has the highest intensity in the marcasite powder pattern, is not consistently observed in the final M1 films as shown by Figure 3.2.

Small concentrations of surfactant relative to the iron source with the M1 method made smoother films made up of small granular crystals and increased film thickness. The ratio of CTAB to Fe^{3+} was 1:2 or 3:4 for this synthesis, Figures 3.10 and 3.11, respectively. Higher temperatures increased the relative amount of the pyrite phase. There was no clear repeatability of the shape of the crystals; crystal shapes in individual films showed significant variation with concentration of the iron source and surfactant. M2 films showed even more variation of crystal size, shape and defects, and very little pyrite phase.

In addition to the difficulty presented by a hydrothermal route – including variation in grain size, shape, and film thickness – for thin film synthesis, another challenge to pyrite's attractiveness as an absorbing layer in a solar cell are electrical properties that have come to light that undermine the attractive optical properties. Conductive surface related defects that result in electrical conductivity of 4 to 5 S/cm make pyrite behave more like a metal than a semiconductor.³⁸ Applications of pyrite phase FeS_2 have shifted from its viability as an absorbing layer in a solar cell to its possible uses for electrocatalysis. Minerals that have the pyrite structure, MX_2 , where M is a transition metal from groups 8 through 12 and X is a chalcogen (S, Se) are promising candidate for their use in the oxygen evolution reactions (OER) and hydrogen evolution reactions (HER).³⁹ Thus, the pyrite thin film synthesis reported in this work may find value as an electrode for photoelectrochemistry and green energy production and these applications are the subject of future work.

5 Future Work

Interrogation of M1 films by atomic force microscopy will be pursued to find the rms roughness and examine the relationship between the concentrations of surfactant and Fe source in their effect on film roughness. In addition, pyrite films will be tested as the working electrode in an electrochemical cell under conditions that promote water oxidation and OER, which is still an area of active research pertinent to water splitting.

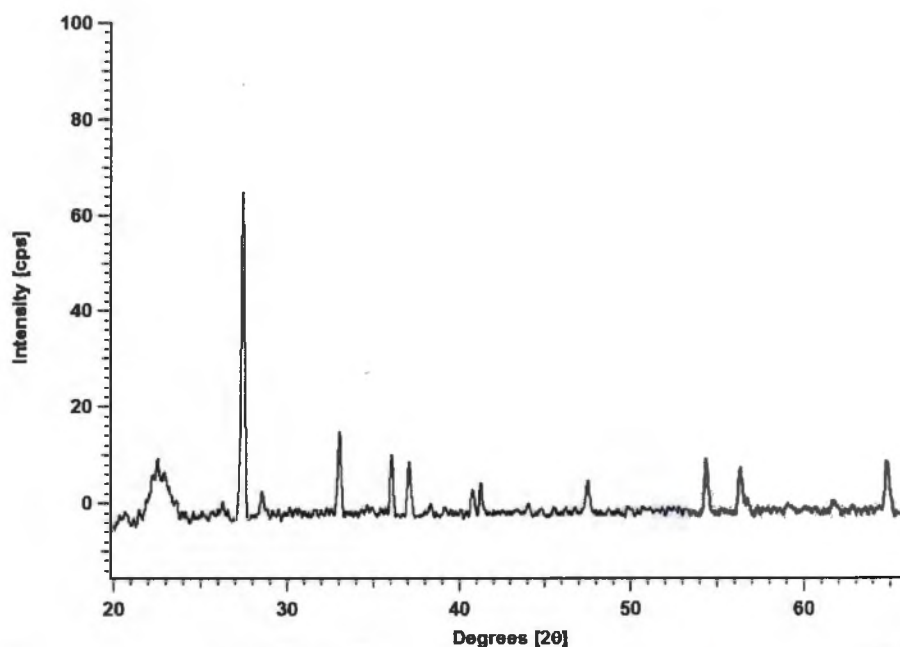
Appendix A

GIXRD Patterns and Peak Details

GIXRD patterns shown with the angle in 2θ , the d value, percent intensity, Miller index and Mineral identity.

Appendix A.1

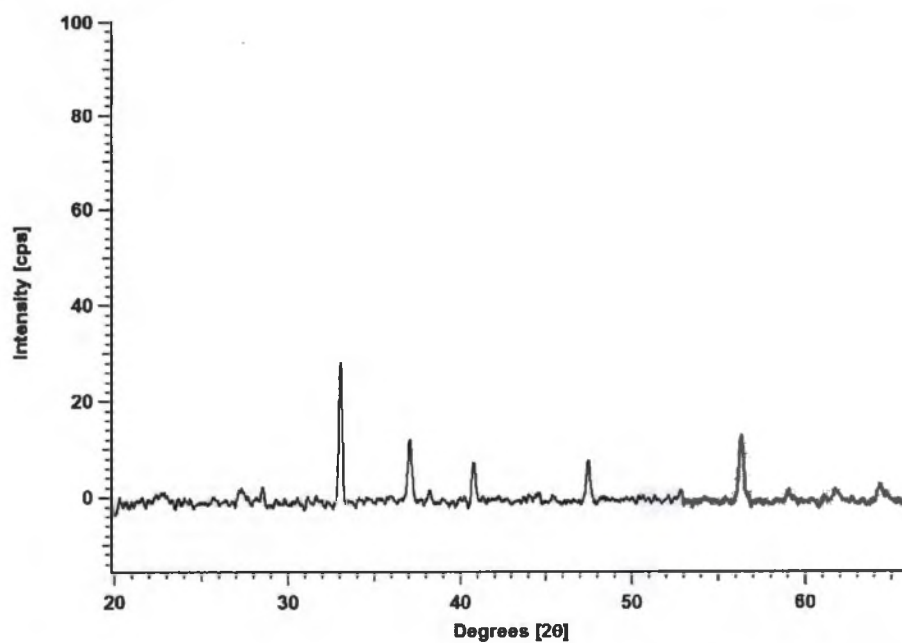
GIXRD of M1 film synthesized with 5 mM precursor, 70 mM CTAB at 230 °C for 1.5 hours.



2θ	d value	Intensity	Intensity %	<i>hkl</i>	Mineral
28.51	3.13	45	62.5	111	P
33.05	2.71	72	100	200	P
37.08	2.42	60	83.3	210	P
40.79	2.21	52	72.2	211	P
47.46	1.91	42	58.3	220	P
56.29	1.63	51	70.8	310	P
59.17	1.56	34	47.2		FeS ₂
61.73	1.50	26	36.1		FeS ₂
64.78	1.44	58	80.6		FeS ₂ , synth

Appendix A.2

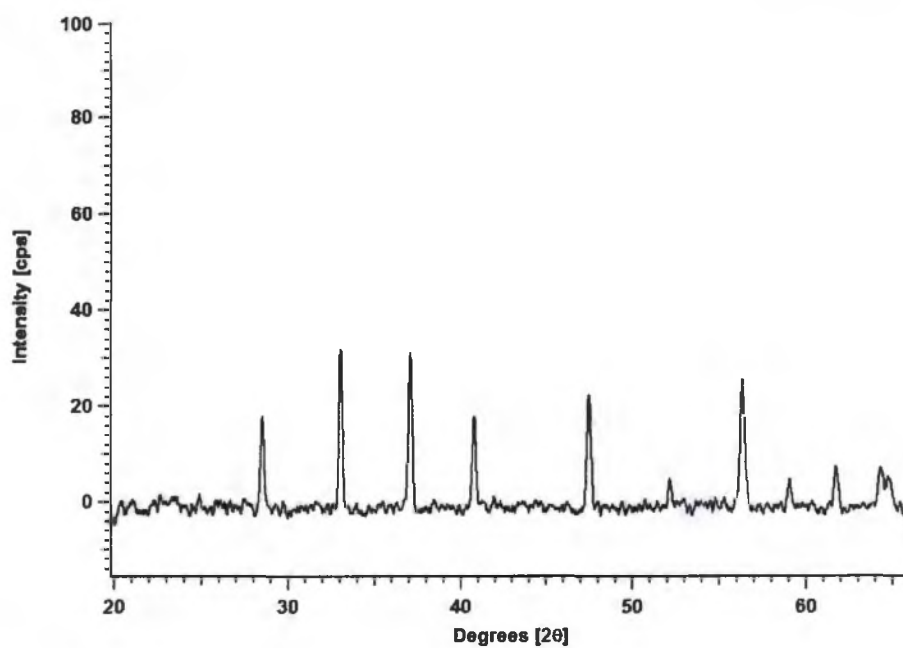
GIXRD of M1 film synthesized with 5.8 mM precursor, 70 mM CTAB at 230 °C for 3 hours.



2θ	d value	Intensity	Intensity %	<i>hkl</i>	Mineral
28.576	3.12121	24	25.3	111	P
33.056	2.70772	95	100	200	P
37.091	2.42192	45	47.4	210	P
40.77	2.21145	35	36.8	211	P
47.488	1.91309	40	42.1	220	P
56.271	1.63353	56	58.9	311	P
58.959	1.5653	28	29.5		FeS ₂
61.481	1.50698	29	30.5		FeS ₂
64.418	1.44519	35	36.8		FeS ₂ , synth

Appendix A.3

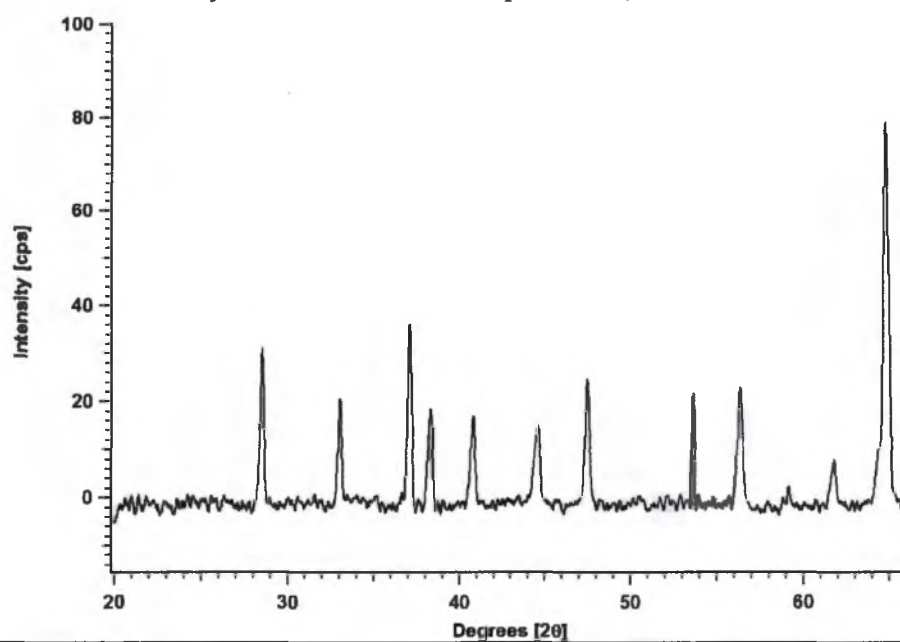
GIXRD of M1 film synthesized with 5.8 mM precursor, 70 mM CTAB at 230 °C for 4.5 hours.



2θ	d value	Intensity	Intensity %	<i>hkl</i>	Mineral
28.54	3.12	29.6	79.7	111	P
33.07	2.71	29.2	78.5	200	P
37.08	2.42	37.2	100	210	P
56.34	1.63	30.4	81.8	311	P
40.80	2.21	24.9	66.9	211	P
47.47	1.91	32.2	86.6	220	P
61.71	1.50	14.9	40.1		FeS ₂

Appendix A.4

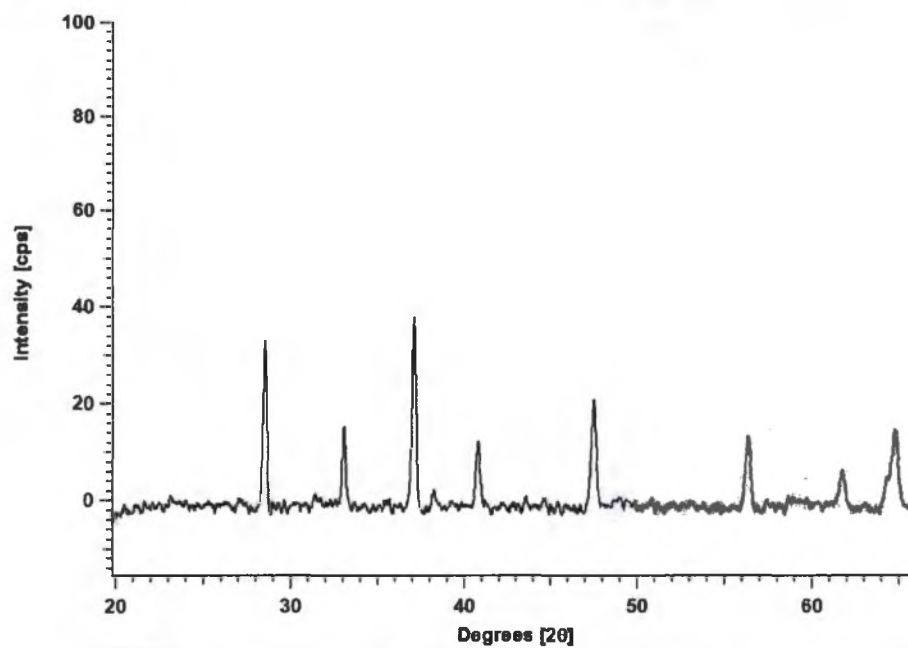
GIXRD of M1 film synthesized with 6 mM precursor, at 230 °C for 1.5 hours.



2θ	d value	Intensity	Intensity %	hkl	Mineral
28.53	3.13	127	52.9	111	P
33.08	2.71	67	27.9	200	P
37.10	2.42	109	45.4	210	P
38.37	2.34	73	30.4		β , FeSO ₄
40.77	2.21	72	30	211	P
44.62	2.03	68	28.3		
47.46	1.91	86	35.8	220	P
50.41	1.81	36	15		UnM, P
56.32	1.63	76	31.7	311	P
59.11	1.56	45	18.8		FeS ₂
61.71	1.50	45	18.8		FeS ₂
64.80	1.44	240	100		FeS ₂ , synth

Appendix A.5

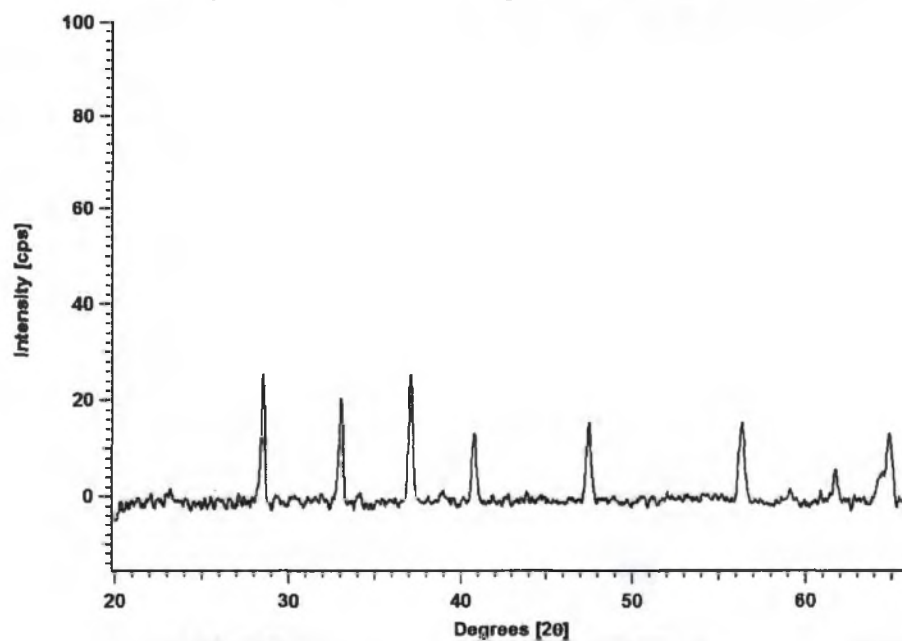
GIXRD of M1 film synthesized with 6 mM precursor, at 230 °C for 3 hours.



$^{\circ}2\theta$	d value	Intensity	Intensity %	<i>hkl</i>	Mineral
28.53	3.13	123	98.4	111	P
33.07	2.71	87	69.6	200	P
37.11	2.42	125	100	210	P
40.76	2.21	64	51.2	211	P
47.46	1.91	90	72	220	P
56.34	1.63	72	57.6	311	P
58.88	1.57	28	22.4		FeS ₂
61.67	1.50	43	34.4		FeS ₂
64.77	1.44	77	61.6		FeS ₂ , synth

Appendix A.6

GIXRD of M1 film synthesized with 6 mM precursor, at 230 °C for 4.5 hours.



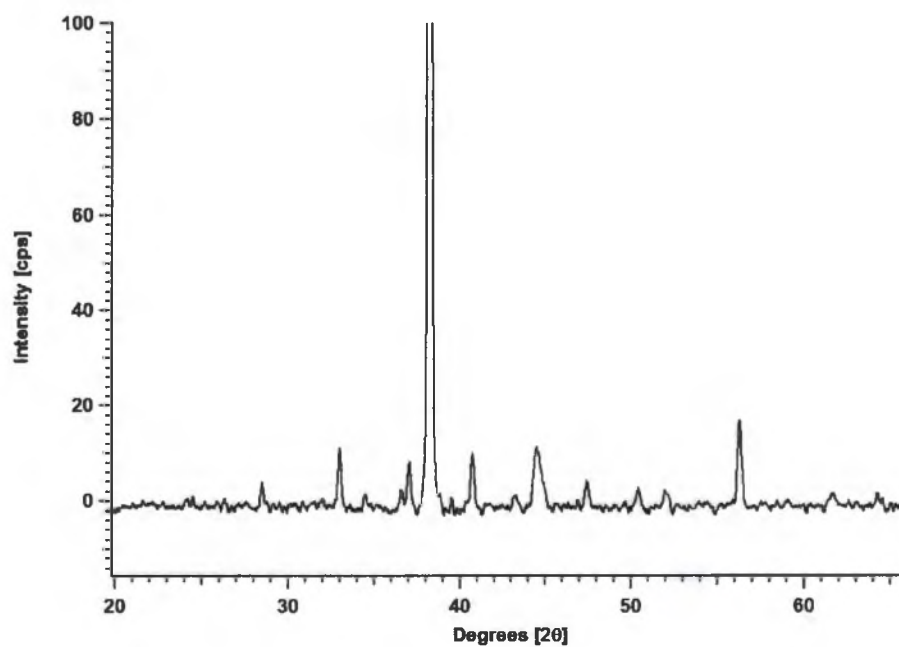
2θ	d value	Intensity	Intensity %	<i>hkl</i>	Mineral
28.52	3.13	118	100	111	P
33.07	2.71	86	72.9	200	P
37.09	2.42	91	77.1	210	P
40.80	2.21	68	57.6	211	P
47.46	1.91	85	72	220	P
56.30	1.63	67	56.8	311	P
59.34	1.56	27	22.9		FeS ₂
61.75	1.50	30	25.4		FeS ₂
64.78	1.44	58	49.2		P

Appendix B

$2\theta - \omega$ patterns shown with the angle in 2θ , the d value, percent intensity, Miller index and Mineral identity.

Appendix B.1

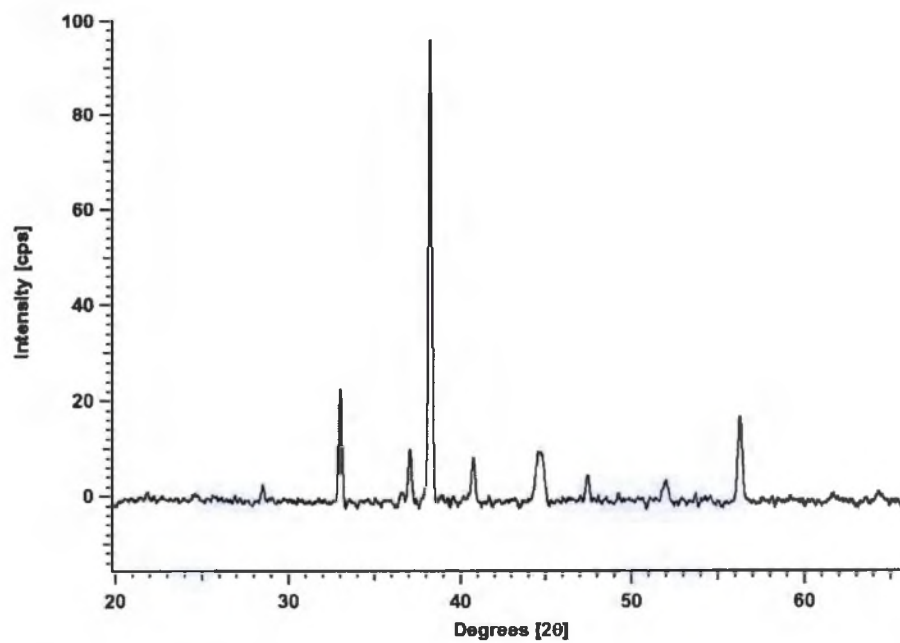
$2\theta - \omega$ XRD pattern of M1 film synthesized with 5 mM precursor, 70 mM CTAB at 230 °C for 1.5 hours.



2θ	d value	Intensity	Intensity %	hkl	Mineral
28.49	3.13	18.4	7.4	111	P
33.05	2.71	21.3	8.6	200	P
36.65	2.45	16	6.4		
37.06	2.42	21.6	8.7	210	P
38.23	2.35	248	100	111	Au
40.79	2.21	24.3	9.8	211	P
44.47	2.04	23.4	9.4	200	Au
47.43	1.92	14.3	5.8	220	P
56.26	1.63	28.6	11.5	311	P

Appendix B.2

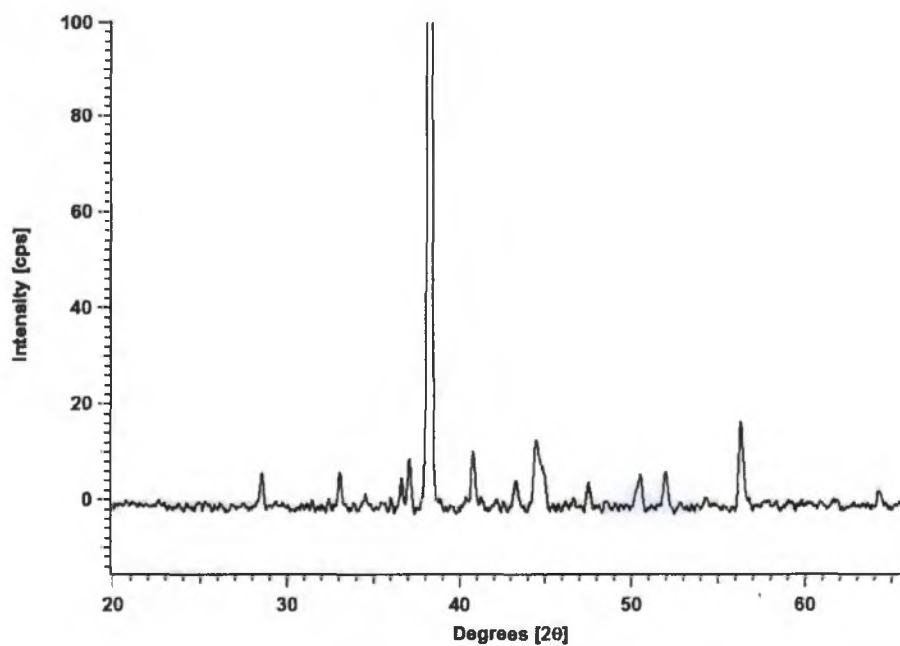
$2\theta - \omega$ XRD pattern of M1 film synthesized with 5.8 mM precursor, 70 mM CTAB at 230 °C for 3 hours.



2θ	d value	Intensity	Intensity %	<i>hkl</i>	Mineral
28.50	3.13	14.7	12.3	111	P
33.06	2.71	33.9	28.6	200	P
37.09	2.42	25.3	21.4	210	P
38.25	2.35	119	100	111	Au
40.77	2.21	24.5	20.7	211	P
44.65	2.03	25.8	21.8		FeS
47.44	1.91	19.8	16.7	220	P
51.99	1.76	15.9	13.4	211	M
56.25	1.63	31.4	26.5	311	P

Appendix B.3

$2\theta - \omega$ XRD pattern of M1 film synthesized with 5.8 mM precursor, 70 mM CTAB at 230 °C for 4.5 hours.



2θ	d value	Intensity	Intensity %	<i>hkl</i>	Mineral
28.54	3.13	19.6	6.5	111	P
33.02	2.71	18.9	6.3	200	P
36.56	2.46	19.4	6.5		W
37.09	2.42	26.3	8.8	210	P
38.25	2.35	301	100	111	Au
40.74	2.21	24.8	8.3	211	P
43.22	2.09	19.1	6.4	111	Cu
44.39	2.04	25.3	8.4	200	Au
44.77	2.02	22.1	7.4		FeS
47.51	1.91	17.9	5.9	220	P
50.49	1.81	20.3	6.7	200	Cu
51.92	1.76	20.9	6.9	211	M
56.29	1.63	34.2	11.4	311	P

References:

- (1) Thomas J. Crowley. Causes of Climate Change Over the Past 1000 Years. *Science* **2000**, 289.
- (2) D. M. Etheridge. Natural and Anthropogenic Changes in Atmospheric CO₂ over the Last 1000 Years from Air in Antarctic Ice and Firn. *J. Geophys. Res.* **1996**, 101 (D2), 4115–4128.
- (3) Foster, G. L.; Royer, D. L.; Lunt, D. J. Future Climate Forcing Potentially without Precedent in the Last 420 Million Years. *Nat. Commun.* **2017**, 8, 14845. <https://doi.org/10.1038/ncomms14845>.
- (4) Canadell, J. G.; Le Quéré, C.; Raupach, M. R.; Field, C. B.; Buitenhuis, E. T.; Ciais, P.; Conway, T. J.; Gillett, N. P.; Houghton, R. A.; Marland, G. Contributions to Accelerating Atmospheric CO₂ Growth from Economic Activity, Carbon Intensity, and Efficiency of Natural Sinks. *Proc. Natl. Acad. Sci.* **2007**, 104 (47), 18866–18870.
- (5) Royal Society (Great Britain). *Ocean Acidification Due to Increasing Atmospheric Carbon Dioxide*; Royal Society: London, 2005.
- (6) Meyer, J.; Riebesell, U. Reviews and Syntheses: Responses of Coccolithophores to Ocean Acidification: A Meta-Analysis. *Biogeosciences* **2015**, 12 (6), 1671–1682. <https://doi.org/10.5194/bg-12-1671-2015>.
- (7) Wadia, C.; Alivisatos, A. P.; Kammen, D. M. Materials Availability Expands the Opportunity for Large-Scale Photovoltaics Deployment. *Environ. Sci. Technol.* **2009**, 43 (6), 2072–2077.
- (8) Goetzberger, A.; Hoffmann, V. U. *Photovoltaic Solar Energy Generation*; Springer series in optical sciences; Springer: Berlin ; New York, 2005.
- (9) Habas, S. E.; Platt, H. A. S.; van Hest, M. F. A. M.; Ginley, D. S. Low-Cost Inorganic Solar Cells: From Ink To Printed Device. *Chem. Rev.* **2010**, 110 (11), 6571–6594. <https://doi.org/10.1021/cr100191d>.
- (10) Xakalashé, B. S.; Tangstad, M. Silicon Processing: From Quartz to Crystalline Silicon Solar Cells. *South. Afr. Pyrometallurgy* **2011**, 2011.
- (11) Lynn, P. A. *Electricity from Sunlight: An Introduction to Photovoltaics*; Wiley: Chichester, 2010.
- (12) Braga, A. F. B.; Moreira, S. P.; Zampieri, P. R.; Bacchin, J. M. G.; Mei, P. R. New Processes for the Production of Solar-Grade Polycrystalline Silicon: A Review. *Sol. Energy Mater. Sol. Cells* **2008**, 92 (4), 418–424. <https://doi.org/10.1016/j.solmat.2007.10.003>.
- (13) Shah, A. V.; Schade, H.; Vanecek, M.; Meier, J.; Vallat-Sauvain, E.; Wyrsh, N.; Kröll, U.; Droz, C.; Bailat, J. Thin-Film Silicon Solar Cell Technology.

- Prog. Photovolt. Res. Appl.* **2004**, *12* (23), 113–142.
<https://doi.org/10.1002/pip.533>.
- (14) Green, M. A.; Emery, K.; Hishikawa, Y.; Warta, W. Solar Cell Efficiency Tables (Version 37). *Prog. Photovolt. Res. Appl.* **2011**, *19* (1), 84–92.
<https://doi.org/10.1002/pip.1088>.
- (15) Munzer; Holdermann, K. T.; Schlosser, R. E.; Sterk, S. Thin Monocrystalline Silicon Solar Cells. *IEEE Trans. ELECTRON DEVICES* **1999**, *46* (10).
- (16) Petter Jelle, B.; Breivik, C.; Drolsum Røkenes, H. Building Integrated Photovoltaic Products: A State-of-the-Art Review and Future Research Opportunities. *Sol. Energy Mater. Sol. Cells* **2012**, *100*, 69–96.
<https://doi.org/10.1016/j.solmat.2011.12.016>.
- (17) Green, M. A. Thin-Film Solar Cells: Review of Materials, Technologies and Commercial Status. *J. Mater. Sci. Mater. Electron.* **2007**, *18* (S1), 15–19.
<https://doi.org/10.1007/s10854-007-9177-9>.
- (18) Yamaguchi, M.; Takamoto, T.; Araki, K. Super High-Efficiency Multi-Junction and Concentrator Solar Cells. *Sol. Energy Mater. Sol. Cells* **2006**, *90* (18–19), 3068–3077. <https://doi.org/10.1016/j.solmat.2006.06.028>.
- (19) Shahrjerdi, D.; Bedell, S. W.; Ebert, C.; Bayram, C.; Hekmatshoar, B.; Fogel, K.; Lauro, P.; Gaynes, M.; Gokmen, T.; Ott, J. A.; et al. High-Efficiency Thin-Film InGaP/InGaAs/Ge Tandem Solar Cells Enabled by Controlled Spalling Technology. *Appl. Phys. Lett.* **2012**, *100* (5), 053901.
<https://doi.org/10.1063/1.3681397>.
- (20) Grätzel, M. Dye-Sensitized Solar Cells. *J. Photochem. Photobiol. C Photochem. Rev.* **2003**, *4* (2), 145–153. [https://doi.org/10.1016/S1389-5567\(03\)00026-1](https://doi.org/10.1016/S1389-5567(03)00026-1).
- (21) Nazeeruddin, M. K.; Baranoff, E.; Grätzel, M. Dye-Sensitized Solar Cells: A Brief Overview. *Sol. Energy* **2011**, *85* (6), 1172–1178.
<https://doi.org/10.1016/j.solener.2011.01.018>.
- (22) Arnon, D. I. The Light Reactions of Photosynthesis. *Proc. Natl. Acad. Sci.* **1971**, *68* (11), 2883–2892.
- (23) Su'ait, M. S.; Rahman, M. Y. A.; Ahmad, A. Review on Polymer Electrolyte in Dye-Sensitized Solar Cells (DSSCs). *Sol. Energy* **2015**, *115*, 452–470.
<https://doi.org/10.1016/j.solener.2015.02.043>.
- (24) Büker, K.; Alonso-Vante, N.; Tributsch, H. Photoelectrochemical Investigations of Complex Formation Phenomena on Oriented N-Pyrite (FeS₂) Crystal Surfaces. *Berichte Bunsenges. Für Phys. Chem.* **1996**, *100* (11), 1808–1813.
<https://doi.org/10.1002/bbpc.19961001109>.
- (25) Ennaoui, A.; Fiechter, S.; Pettenkofer, C.; Alonso-Vante, N.; Büker, K.; Bronold, M.; Höpfner, C.; Tributsch, H. Iron Disulfide for Solar Energy Conversion. *Sol. Energy Mater. Sol. Cells* **1993**, *29* (4), 289–370.
- (26) Wächtershäuser, G. Evolution of the First Metabolic Cycles. *Proc. Natl. Acad. Sci.* **1990**, *87* (1), 200–204.

- (27) Takahashi, N.; Nakatani, Y.; Yatomi, T.; Nakamura, T. Growth of Single-Crystal Pyrite Films by Atmospheric Pressure Chemical Vapor Deposition. *Chem. Mater.* **2003**, *15* (9), 1763–1765. <https://doi.org/10.1021/cm0210243>.
- (28) Hu, Y.; Zheng, Z.; Jia, H.; Tang, Y.; Zhang, L. Selective Synthesis of FeS and FeS₂ Nanosheet Films on Iron Substrates as Novel Photocathodes for Tandem Dye-Sensitized Solar Cells. *J. Phys. Chem. C* **2008**, *112* (33), 13037–13042. <https://doi.org/10.1021/jp803726c>.
- (29) Liu, Y. H.; Meng, L.; Zhang, L. Optical and Electrical Properties of FeS₂ Thin Films with Different Thickness Prepared by Sulfurizing Evaporated Iron. *Thin Solid Films* **2005**, *479* (1–2), 83–88. <https://doi.org/10.1016/j.tsf.2004.11.147>.
- (30) Timonen, J. V. I.; Seppälä, E. T.; Ikkala, O.; Ras, R. H. A. From Hot-Injection Synthesis to Heating-Up Synthesis of Cobalt Nanoparticles: Observation of Kinetically Controllable Nucleation. *Angew. Chem. Int. Ed.* **2011**, *50* (9), 2080–2084. <https://doi.org/10.1002/anie.201005600>.
- (31) Puthussery, J.; Seefeld, S.; Berry, N.; Gibbs, M.; Law, M. Colloidal Iron Pyrite (FeS₂) Nanocrystal Inks for Thin-Film Photovoltaics. *J. Am. Chem. Soc.* **2011**, *133* (4), 716–719. <https://doi.org/10.1021/ja1096368>.
- (32) Puthussery, J.; Seefeld, S.; Berry, N.; Gibbs, M.; Law, M. *Supporting Information for “Colloidal Iron Pyrite (FeS₂) Nanocrystal Inks for Thin Film Photovoltaics”*; Supplemental Information; University of California, Irvine: Department of Chemistry and Department of Chemical Engineering and Materials Science; pp s1–s9.
- (33) Wu, R.; Zheng, Y. F.; Zhang, X. G.; Sun, Y. F.; Xu, J. B.; Jian, J. K. Hydrothermal Synthesis and Crystal Structure of Pyrite. *J. Cryst. Growth* **2004**, *266* (4), 523–527. <https://doi.org/10.1016/j.jcrysgro.2004.02.020>.
- (34) Wadia, C.; Wu, Y.; Gul, S.; Volkman, S. K.; Guo, J.; Alivisatos, A. P. Surfactant-Assisted Hydrothermal Synthesis of Single Phase Pyrite FeS₂ Nanocrystals. *Chem. Mater.* **2009**, *21* (13), 2568–2570. <https://doi.org/10.1021/cm901273v>.
- (35) Levlin, M.; Laakso, A.; Niemi, H. E.-M.; Hautojärvi, P. Evaporation of Gold Thin Films on Mica: Effect of Evaporation Parameters. *Appl. Surf. Sci.* **1997**, *115* (1), 31–38. [https://doi.org/10.1016/S0169-4332\(96\)00851-3](https://doi.org/10.1016/S0169-4332(96)00851-3).
- (36) Boston Consolidated Mine, Bingham Canyon, 20 Mi SSW of Salt Lake City, Salt Lake County, Utah, USA. ruff.
- (37) Brostigen, G.; Kjekshus, A.; Astrup, E. E.; Nordal, V.; Lindberg, A. A.; Craig, J. C. Redetermined Crystal Structure of FeS₂ (Pyrite). *Acta Chem. Scand.* **1969**, *23*, 2186–2188. <https://doi.org/10.3891/acta.chem.scand.23-2186>.
- (38) Steinhagen, C.; Harvey, T. B.; Stolle, C. J.; Harris, J.; Korgel, B. A. Pyrite Nanocrystal Solar Cells: Promising, or Fool’s Gold? *J. Phys. Chem. Lett.* **2012**, *3* (17), 2352–2356. <https://doi.org/10.1021/jz301023c>.

- (39) Gao, M.-R.; Zheng, Y.-R.; Jiang, J.; Yu, S.-H. Pyrite-Type Nanomaterials for Advanced Electrocatalysis. *Acc. Chem. Res.* **2017**, *50* (9), 2194–2204. <https://doi.org/10.1021/acs.accounts.7b00187>.